Geochemistry
Geophysics
Geosystems
G^3
AN ELECTRONIC JOURNAL OF THE EARTH SCIENCES
Published by AGU and the Geochemical Society

Article
Volume 5, Number 12
15 December 2004
Q12007, doi:10.1029/2004GC000764
ISSN: 1525-2027

Tectonic/volcanic segmentation and controls on hydrothermal venting along Earth's fastest seafloor spreading system, EPR 27°–32°S

Richard Hey
School of Ocean and Earth Science and Technology, University of Hawaii, 2525 Correa Road, Honolulu, Hawaii 96822, USA (hey@soest.hawaii.edu)

Edward Baker
NOAA/Pacific Marine Environmental Laboratory, 7600 Sand Point Way N.E., Seattle, Washington 98115-0070, USA

DelWayne Bohnenstiehl
Lamont-Doherty Earth Observatory of Columbia University, 61 Route 9W, Palisades, New York 10964, USA

Gary Massoth
Institute of Geological and Nuclear Sciences, Ltd., 30 Gracefield Road, P.O. Box 31-312, Lower Hutt, New Zealand

Martin Kleinrock
Joint Oceanographic Institutions, Inc., 1201 New York Ave, NW, Suite 400, Washington, DC 20005, USA

Fernando Martinez
School of Ocean and Earth Science and Technology, University of Hawaii, 2525 Correa Road, Honolulu, Hawaii 96822, USA

David Naar
College of Marine Science, University of South Florida, 140 Seventh Avenue South, St. Petersburg, Florida 33701-5016, USA

Debra Pardee
School of Ocean and Earth Science and Technology, University of Hawaii, 2525 Correa Road, Honolulu, Hawaii 96822, USA

Now at URS Corporation, 615 Piikoi Street, Suite 900, Honolulu, Hawaii 96814, USA

John Lupton
NOAA/Pacific Marine Environmental Laboratory, 2115 SE OSU Drive, Newport, Oregon 97365, USA

Richard Feely
NOAA/Pacific Marine Environmental Laboratory, 7600 Sand Point Way N.E., Seattle, Washington 98115-0070, USA

Jim Gharib
School of Ocean and Earth Science and Technology, University of Hawaii, 2525 Correa Road, Honolulu, Hawaii 96822, USA

Joe Resing
NOAA/Pacific Marine Environmental Laboratory, 7600 Sand Point Way N.E., Seattle, Washington 98115-0070, USA

Also at Joint Institute for the Study of the Atmosphere and the Ocean, University of Washington, Seattle, Washington, USA

Cristian Rodrigo
Servicio Hidrografico y Oceanografico de la Armada de Chile, Errazuriz 232 Playa Ancha, Valparaiso, Chile

Francis Sansone
School of Ocean and Earth Science and Technology, University of Hawaii, 2525 Correa Road, Honolulu, Hawaii 96822, USA

Sharon Walker
NOAA/Pacific Marine Environmental Laboratory, 7600 Sand Point Way N.E., Seattle, Washington 98115-0070, USA

[1] We have collected 12 kHz SeaBeam bathymetry and 120 kHz DSL-120 side-scan sonar and bathymetry data to determine the tectonic and volcanic segmentation along the fastest spreading (~150 km/Myr) part of the global mid-ocean ridge system, the southern East Pacific Rise between the Easter and Juan Fernandez microplates. This area is presently reorganizing by large-scale dueling rift propagation and possible protomicroplate tectonics. Fracture patterns observed in the side-scan data define structural segmentation scales along these ridge segments. These sometimes, but not always, correlate with linear volcanic systems defining segmentation in the SeaBeam data. Some of the subsegments behave cohesively, with in-phase tectonic activity, while fundamental discontinuities occur between other subsegments. We also collected hydrothermal plume data using sensors mounted on the DSL-120 instrument package, as well as CTDO tow-yos, to determine detailed structural and volcanic controls on the hydrothermal vent pattern observed along 600 km of the Pacific-Nazca axis. Here we report the first rigorous correlation between coregistered hydrothermal plume and high-resolution marine geophysical data on similar scales and over multisegment distances. Major plume concentrations were usually found where axial inflation was relatively high and fracture density was relatively low. These correlations suggest that hydrothermal venting is most active where the apparent magmatic budget is greatest, resulting in recent eruptions that have paved over the neovolcanic zone. Areas of voluminous acoustically dark young lava flows produced from recent fissure eruptions correlate with many of the major hydrothermal vent areas. Increased crustal permeability, as gauged by increased fracture density, does not enhance hydrothermal venting in this area. Axial summit troughs and graben are rare, probably because of frequent volcanic resurfacing in this superfast spreading environment, and are not good predictors of hydrothermal activity here. Many of the hydrothermal areas are found in inflated areas near the ends of segments, suggesting that abundant magma is being supplied to these areas.

Components: 15,313 words, 12 figures, 1 table.

Keywords: seafloor spreading; mid-ocean ridges; hydrothermal plumes.

Index Terms: 3035 Marine Geology and Geophysics: Midocean ridge processes; 3045 Marine Geology and Geophysics: Seafloor morphology and bottom photography; 3094 Marine Geology and Geophysics: Instruments and techniques; 4832 Oceanography: Biological and Chemical: Hydrothermal systems; 8150 Tectonophysics: Plate boundary—general (3040)

Received 25 May 2004; **Revised** 3 September 2004; **Accepted** 21 October 2004; **Published** 15 December 2004.

Hey, R., et al. (2004), Tectonic/volcanic segmentation and controls on hydrothermal venting along Earth's fastest seafloor spreading system, EPR 27°–32°S, *Geochem. Geophys. Geosyst.*, *5*, Q12007, doi:10.1029/2004GC000764.

1. Introduction

[2] Earth's fastest present-day seafloor spreading, as measured by magnetic anomalies, occurs along the southern East Pacific Rise (EPR), along the Pacific-Nazca plate boundary [e.g., *DeMets et al.*, 1990, 1994]. Here we describe the tectonic and volcanic segmentation along the fastest spreading part of this ridge, and discuss detailed structural and volcanic controls on the hydrothermal vent pattern observed along 600 km of the southern EPR

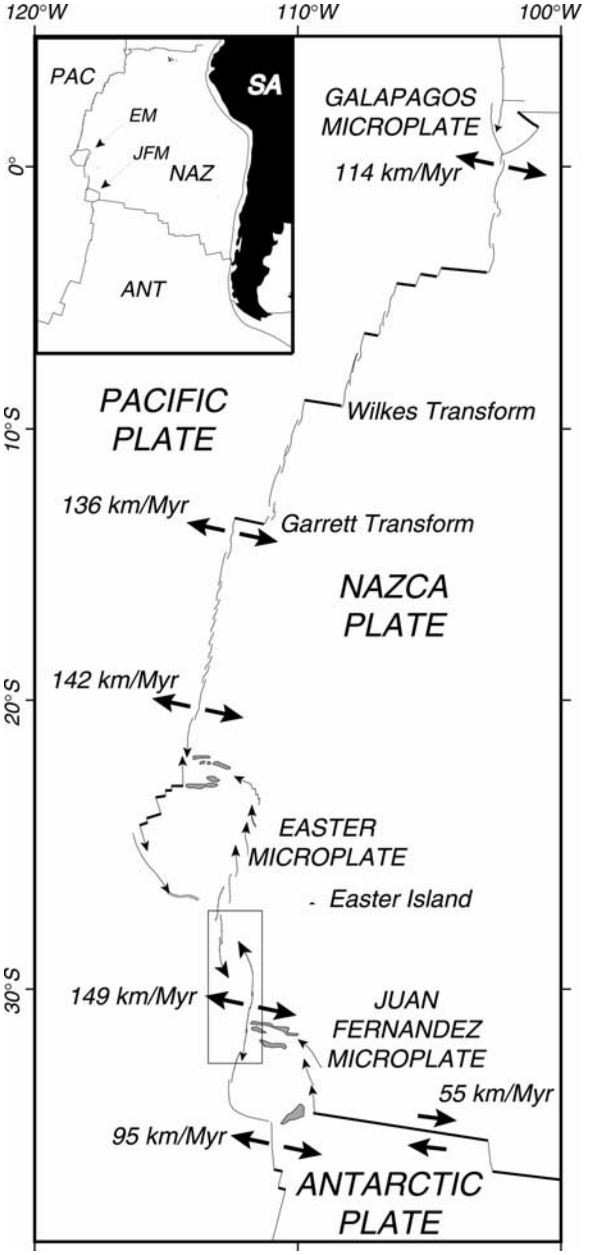

Figure 1. Location map and spreading rates from *Hey et al.* [1995]. Light lines are mid-ocean ridges; those with arrows are propagating. Heavy straight lines are transform faults. Box surrounds axes surveyed.

(*Baker et al.* [2002] and new results reported here).

[3] Figure 1 shows that a qualitative change in EPR plate boundary geometry occurs somewhere between the Garrett transform fault at 13°S and the dueling propagators near 21°S. Between the Garrett and the Pacific-Nazca-Cocos triple junction the usual ridge/transform geometry dominates, with even the intratransform spreading center patterns predictable from known changes in plate motion [*Searle*, 1983; *Fox and Gallo*, 1984; *Lonsdale*, 1989]. In contrast, the entire part of the Pacific-Nazca boundary spreading faster than 142 km/Myr is reorganizing by propagating rift and microplate tectonics [*Naar and Hey*, 1989a]. At these faster spreading rates, detailed swath mapping has shown there are no transform faults, but rather various nontransform offsets, including he 21°S dueling propagators [*Macdonald et al.*, 1988a], the Easter and Juan Fernandez microplates [*Hey et al.*, 1985; *Searle et al.*, 1989; *Naar and Hey*, 1991; *Larson et al.*, 1992; *Rusby and Searle*, 1995; *Bird et al.*, 1998] and the giant dueling propagators between these microplates [*Hey et al.*, 1995; *Korenaga and Hey*, 1996]. Transform faults do not occur again (other than transient ones on the slower spreading microplate boundaries) until the spreading rate drops at the triple junction south of the Juan Fernandez microplate (Figure 1).

[4] The spreading rates in Figure 1 [from *Hey et al.*, 1995] were calculated using the revised astronomically calibrated magnetic timescale [*Shackleton et al.*, 1990; *Hilgen*, 1991] to modify the *Naar and Hey* [1989b] Pacific-Nazca Brunhes pole. This pole was constrained by EPR magnetic anomaly data collected too late for the NUVEL-1 compilation, and so, although similar, is an improvement to the best-fitting PAC-NAZ pole from NUVEL-1 [*DeMets et al.*, 1990]. NUVEL-1A [*DeMets et al.*, 1994] also uses the revised timescale, but is a global plate motion model, contaminated by errors elsewhere, that predicts faster spreading than observed along the Pacific-Nazca boundary. In addition to fitting the new data better along the fastest part of this ridge, the *Hey et al.* [1995] pole (48.1°N, 90.5°W, 1.35°/Myr) also provides a better fit to the 18°–19°S EPR data than the NUVEL models [*Cormier and Macdonald*, 1994, Figure 13]. Thus the spreading rates shown in Figure 1 are the most accurate currently available for this region, and a fundamental change in plate boundary behavior occurs between spreading (whole) rates of 136 and 142 km/Myr, which we use to define a distinction between fast and "superfast" spreading behavior. We prefer this terminology to that including slower spreading areas such as the 17°S MELT area (~140 km Myr) in an "ultrafast" spreading category, especially as *Wilson* [1996] has shown there were faster spreading rates in the Miocene on the Pacific-Cocos ridge.

[5] Here we document both large-scale and finer-scale segmentation patterns along this fastest spreading ridge based on new SeaBeam and DSL-120 data, and the structural controls on the hydrothermal plume patterns in the area.

2. Techniques

[6] Hull-mounted SeaBeam 2000 multibeam bathymetry data were collected during the 1993 GLORIA05 and 1998 PANORAMA05 R/V *Melville* expeditions, on a series of along and across axis track lines within the 27°–32°S region of the EPR. The SeaBeam 2000 mapping system operates at 12 kHz with 121 across-track beams forming a 120° swath, generating an ∼8–10 km wide swath of bathymetric data (3.5 × water depth) throughout the survey area. Along the crest of the axial high, higher-resolution bathymetry and side-scan sonar imagery also were collected using the DSL-120 system. The DSL-120 is a 120 kHz phase-difference sonar system, which generates acoustic backscatter imagery and coregistered bathymetry over typical swath widths of 1.0 and 0.7 km, respectively. Throughout the survey, the instrument package was towed essentially parallel to the spreading axis at an altitude of ∼0.1 km above the seafloor and a speed of ∼1.5–1.7 kt (∼0.8 m/s). Using a standard layback correction, the instrument was navigated relative to the ship location, which was determined using P-code Global Positioning System (GPS) information.

[7] The DSL-120 system incorporates an ∼2 m^2 area of seafloor into each measurement, with an across-track sampling dimension of only 0.13–0.33 m [*Stewart et al.*, 1994; *Scheirer et al.*, 2000]. These raw data were gridded at a 2 × 2 m resolution, and a 10-m boxcar filter was applied to the bathymetric data in order to remove spurious data points. The gridded backscatter imagery is sensitive to track-parallel scarps of submeter width, and the gridded bathymetry, which is routinely contoured at an interval of 5 m, has a vertical resolution on the order of 1–2 m [*Bohnenstiehl and Kleinrock*, 1999; *Scheirer et al.*, 2000]. Morphologic features were identified and digitized on the basis of the analysis of the coregistered DSL-120 sonar imagery and bathymetric data. Fault scarps are characterized by the steepness of their slopes in the bathymetric data and by linear regions of high-amplitude backscatter or acoustic shadow in the sonar imagery, depending on their dip direction relative to the DSL-120 instrument package (in our images, light areas are relatively high side-scan backscatter, and dark/black areas are low backscatter or acoustic shadows). Due to the subjectivity associated with defining the center of the axis in many areas, we made no attempt to identify inward versus outward dipping structures [cf. *Bohnenstiehl and Carbotte*, 2001]. Fissures, which are narrow-walled cracks with no discernable vertical offset, are manifested in the sonar imagery as narrow bands of adjacent acoustic shadow and high amplitude backscatter. Large-scale collapse features were identified from their bathymetric relief and steep sided walls. In some instances, individual lava flows could be identified due to their distinctive backscatter characteristics and the steepness of the flow front.

[8] The distribution of seafloor vent sources was inferred using two plume-mapping techniques. A conductivity-temperature-depth-optical (CTDO) package was towed along the ridge axis in a sawtooth (tow-yo) pattern to continuously map hydrothermally derived temperature and light backscattering (in terms of nephelometric turbidity units (ΔNTU) determined from a laboratory calibration using formazine [*Baker et al.*, 2001]) anomalies, as described by *Baker et al.* [2002]. The sawtooth wavelength was typically 1–2 km and the CTDO was cycled between 20 m above bottom (mab) and the top of any observed plume horizon, ∼300–400 mab. Here we vertically integrate the light backscattering data ($\sum\Delta$NTU) by first gridding the data into cells measuring 0.03° of latitude (∼3 km) by 25 m vertically, then summing the cells in each latitude bin. This technique yields an along-axis plume inventory, identifying spatial patterns of seafloor discharge and simplifying a comparison to the along-axis distribution of fractures, flows, and collapse areas.

[9] A finer-scale indication of the distribution of seafloor vents was obtained from an optical sensor and an in situ chemical analyzer (SUAVE) mounted on the DSL-120 depressor weight, ∼100 mab. SUAVE continuously measured dissolved Mn (DMn) as described by *Massoth et al.* [1998], modified here to accommodate a slower pump speed for a lower detection limit (<5 nM Mn). Instrument response time for a 150 nM signal was ∼2.8 min, equivalent to ∼130 m of towpath at a DSL tow speed of 1.5 kt. Discrete samples from CTDO/SUAVE casts were used for calibrations [*Baker et al.*, 2002]. Unlike the CTDO data, the SUAVE optical and chemical data are exactly coregistered in time and space with the side-scan

imagery. More importantly, sensors on the side scan produce a continuous and high-resolution record of hydrothermal anomalies at a fixed depth above bottom, simplifying the interpretative connection between plumes and seafloor. Additional optical sensors were attached above and below the DSL-120, but *Walker et al.* [2004] show that SUAVE passed through all plumes detected by this optical sensor array. *Walker et al.* [2004] also show that the plume distribution as imaged by CTDO tow-yo and the DSL array are quite similar, though near-bottom currents can advect plumes up to ~10 km along axis over a period of a few days. Without knowing the precise locations of the seafloor discharges we cannot determine which plume distribution is most accurate, but having two separate realizations of the distribution allows a more confident linkage of the plume and side-scan data sets.

3. Ridge Segmentation on the SeaBeam Scale

[10] There are several fundamental scales of ridge segmentation [e.g., *Macdonald et al.*, 1988b, 1991; *Forsyth*, 1992; *Batiza*, 1996] including the plate scale, where ridge systems are segmented by triple junctions (on this scale it is significant that the Pacific-Nazca ridge has the fastest active spreading), and the ocean basin scale (where it is significant that the active Pacific spreading centers range from medium to fast while the Atlantic spreading centers are slow). In this local area, the axial segmentation pattern is dominated by the "dueling propagator" competition between the Pacific-Nazca ridge segments between the Easter and Juan Fernandez microplates [*Hey et al.*, 1995; *Korenaga and Hey*, 1996]. This has been a one-sided duel, with the West ridge lengthening over the past 1.5–2 Ma, propagating south at an average velocity of about 135 km/Myr, although there have been occasional brief episodes of northward propagation of the failing East ridge, as shown by characteristic failed rift signatures in the seafloor backscatter, bathymetry, structural, and magnetic patterns [*Naar and Hey*, 1991; *Klaus et al.*, 1991; *Bird and Naar*, 1994; *Hey et al.*, 1995; *Korenaga and Hey*, 1996]. The most recent episode of dueling propagation has extended the East ridge north about 120 km during the past 0.2–0.3 Ma, creating a large and pervasively deformed overlap zone. Both the Easter microplate to the north and Juan Fernandez microplate to the south have pervasively deformed cores [*Hey et al.*, 1985; *Searle et al.*, 1989; *Larson et al.*, 1992], so this giant overlap zone may be an initial stage of microplate formation [*Hey et al.*, 1995]. The scale of this overlap zone (~120 × 120 km) and greater than 300 km lengths of both the East and West ridges indicates that, according to the local-scale terminology of *Macdonald et al.* [1991] and *White et al.* [2000], the East and West ridges are the only two first-order segments in this area, separated by a first-order discontinuity, the giant overlap zone, although one that changes geometry and position.

[11] At a smaller scale, the segmentation of the ridge axis is defined by separate linear axial volcanic systems, which are similar to those found on the EPR north of the Easter microplate [*Macdonald et al.*, 1991; *White et al.*, 2000]. We have surveyed six of these major active segments and two others bounding part of the giant overlap zone where spreading, although clearly recently active, may have stopped very recently on parts of the dueling propagators. These segments are typically bounded by small nontransform discontinuities, where competing axial volcanic rift zones fail to intersect by a few km, usually at some kind of overlapping spreading center (OSC) [e.g., *Macdonald and Fox*, 1983; *Lonsdale*, 1983]. In the *Macdonald et al.* [1991] and *White et al.* [2000] terminology, these separate linear volcanic systems would be second-order segments separated by second-order discontinuities. Here we modify the *Hey et al.* [1995] interpretation and terminology of this segmentation pattern (Figures 2 and 3; Table 1).

3.1. West Ridge

[12] Although there are additional segments (W1 and W2) to the north, connecting this ridge to the East ridge of the Easter microplate, our 1998 investigation began near 27°30′S on segment W3. Segment W1 is the shallowest and most inflated segment of the Easter microplate East Rift, and segment W2 is also highly inflated [*Martinez et al.*, 1997; *Pardee et al.*, 2000]. Both are part of the southward propagating West ridge system [*Schilling et al.*, 1985; *Naar and Hey*, 1991]. Figure 2 shows an overall plunge in axial depth along the West ridge system toward the south, ~600 m in 300 km, an average slope of 0.1°, and a similar pattern of reduced inflation to the south, a decrease of ~400 m^2/m, consistent with southward "downhill" propagation [*Hey et al.*, 1980; *Phipps Morgan and Parmentier*, 1985]. Segment W1 also is propagating north [*Hey et al.*, 1985; *Naar and Hey*, 1986], lengthening in both directions (Figure 1), and at its northern tip is

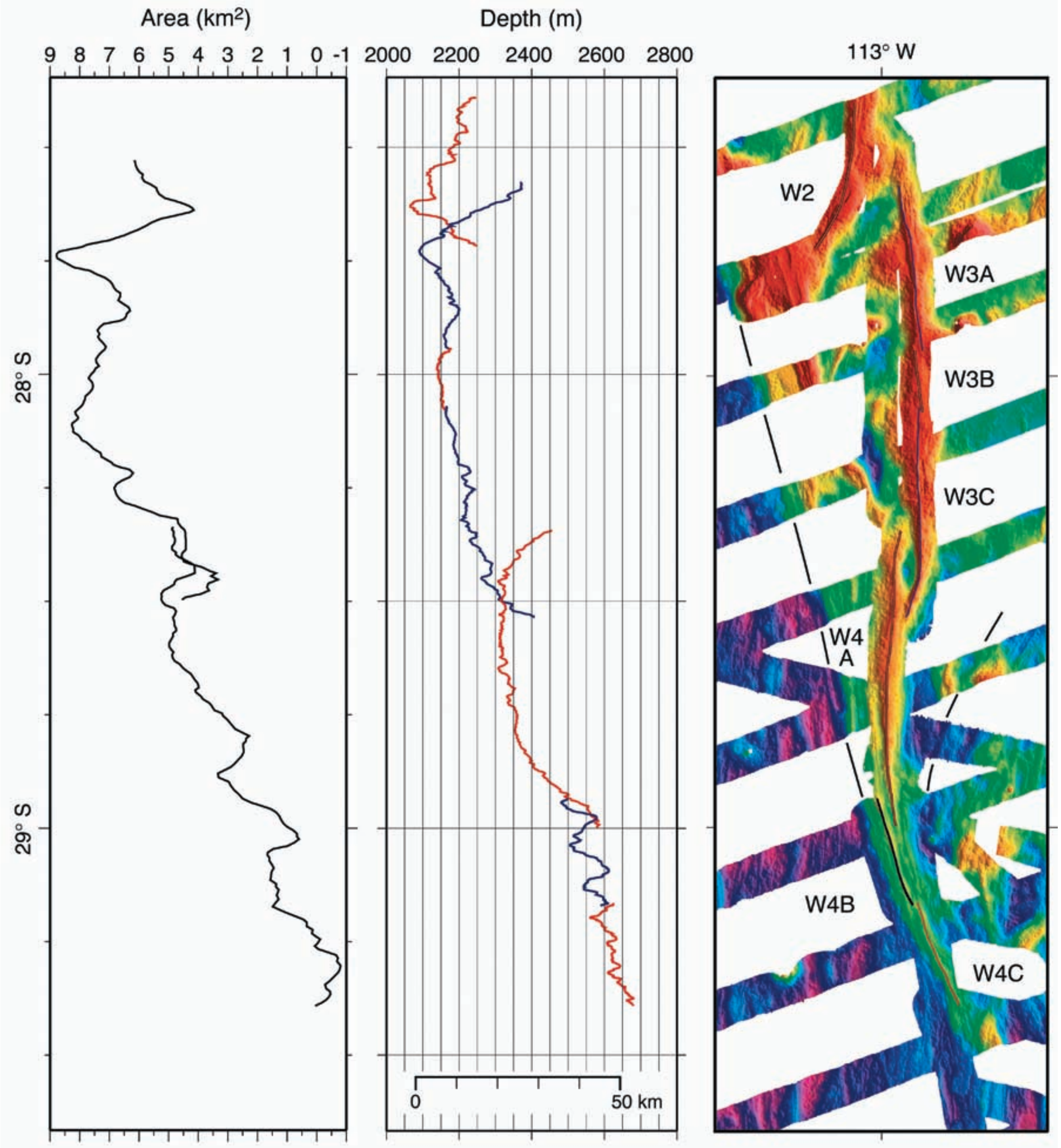

Figure 2. West ridge patterns of depth and inflation. Subsegments (W3A, etc.) defined by SeaBeam bathymetry. Dashed lines between SeaBeam tracks show pseudofaults [*Hey*, 1977] of southward propagating West ridge system.

the dominant active propagator in the series of northward propagators that created the Easter microplate beginning ~5 Ma [*Naar and Hey*, 1991]. Both of these major W1 propagators are propagating downhill away from the shallowest Easter microplate segment, nearest Easter Island, with the highest He 3/4 ratio in dredged rock samples [*Poreda et al.*, 1993]. This is the ridge segment most influenced by what seems to be an enigmatic Easter mantle plume. Geochemically, this plume appears to be located at Salas y Gomez Island [*Schilling et al.*, 1985; *Hanan and Schilling*, 1989], but seismically it is seen to rise from the core-mantle boundary to the surface near Easter Island [*Montelli et al.*, 2004], and it creates excess volcanism over a broad area.

[13] The W2/W3 discontinuity is a peculiar nontransform offset (Figures 2 and 4). The spreading axes overlap by at least 16 km, but instead of the classic OSC curvature of the axes toward each other, the southern tip of W2 curves strongly away

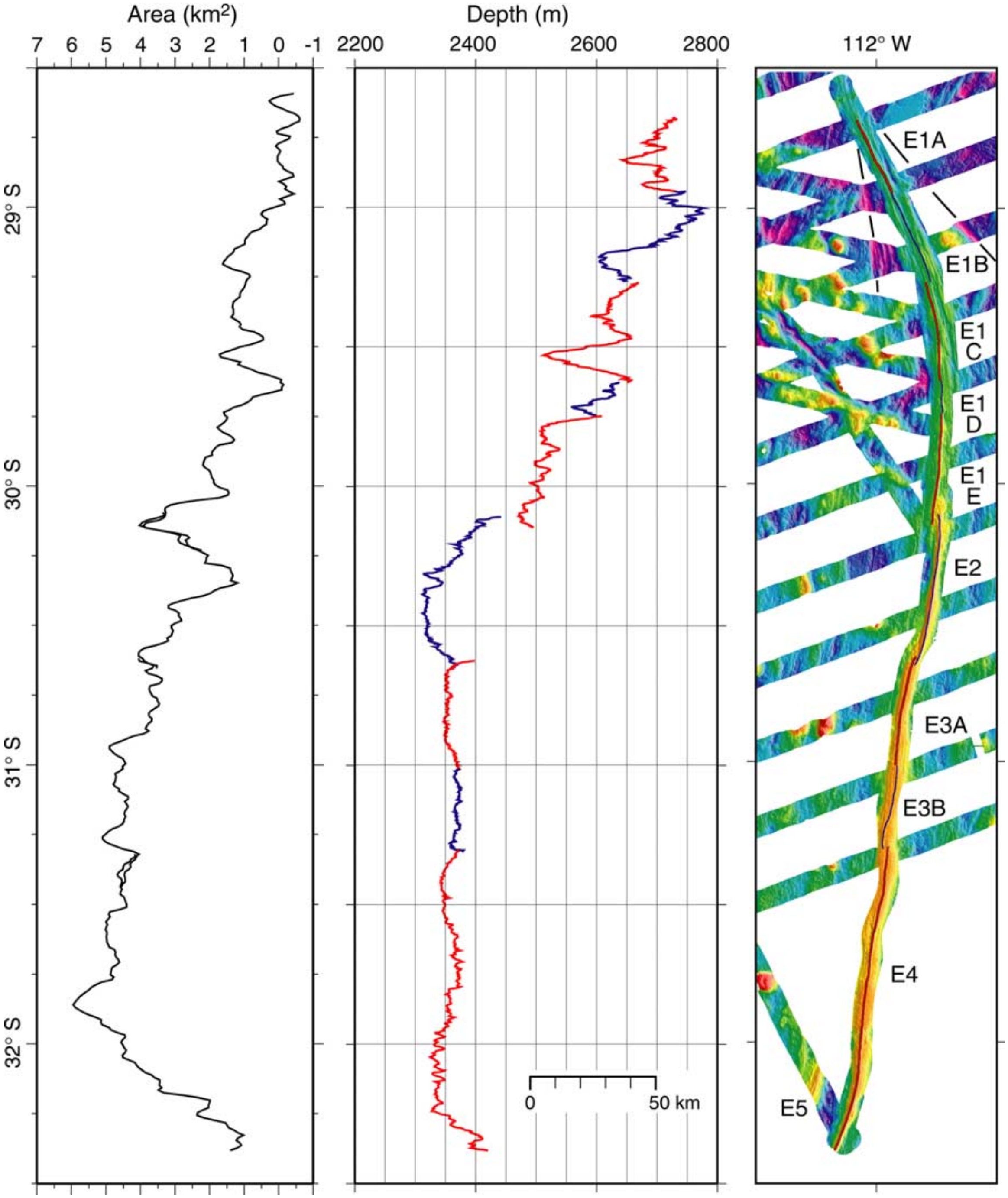

Figure 3. East ridge patterns of depth and inflation. Subsegments (E1A, etc.) defined by SeaBeam bathymetry. Inflation pattern from *Martinez et al.* [1997]. Dashed lines between SeaBeam tracks show pseudofaults of northward propagating East ridge system.

from the northern tip of W3. W2 ends at the outer pseudofault [*Hey*, 1977] of the West ridge propagator wake at the shallowest point (~2000 m) along the pseudofault. At this intersection, there is a ridge subparallel to the pseudofault that has rift structures evident in the SeaBeam data (Figure 2), and the same elevation and morphological shape as the nearby spreading axes. Data gaps preclude a confident interpretation, but this might be an unusual extinct axis replaced by W3, or possibly an even more unusual active spreading axis [*Johnson*, 1996].

Table 1. Ridge Segmentation Pattern Defined by SeaBeam Bathymetry

Discontinuity	Latitude, °S	L or R Stepping	Offset Width, km	Overlap Length, km	Type
W2/W3A	27°34.5′–27°43.0′	L	17.2	16.8	nontraditional OSC, W2 curves wrong way, away from W3
W3A/W3B	27°56.6′	R	1.8	0	nonintersecting rift zones
W3B/W3C	28°04.2′–28°04.8′	R	0.7	1.0	nonintersecting rift zones
W3C/W4A	28°20.7′–28°32.1′	R	6.5	21.1	OSC (deep overlap basin)
W4A/W4B	28°55.9′–28°59.9′	R	3	7.8?	nonintersecting rift zones
W4B/W4C	29°10.0′–29°10.2′	L	1.3	0	nonintersecting rift zones
E1A/E1B	28°56.6′	R	0.3	0	nonintersecting rift zones
E1B/E1C	29°16.0′	R	2	0	nonintersecting rift zones
E1C/E1D	29°37.6′	L	0.5	0	nonintersecting rift zones
E1D/E1E	29°44.9′	R	0.4	0	nonintersecting rift zones
E1E/E2A	30°06.6′–30°08.8′	L	2.7	4.2	OSC (essentially no overlap basin)
E2A/E2B	30°19.9′	R	0.3	0	nonintersecting rift zones
E2B/E3A	30°37.5′–30°39.3′	R	1.3	3.3	OSC (essentially no overlap basin)
E3A/E3B	31°00.8′	L	0.6	0	nonintersecting rift zones
E3B/E4A	31°18.3′–31°18.7′	L	2	1	OSC (very small overlap basin)
E4A/E4B	31°36.2′	R	0.2	0	inflation boundary/nonintersecting rift zones
E4B/E4C	~31°46.5′	N/A	0	0	inflation boundary
E4C/E4D	~31°58.0′	N/A	0	0	inflation boundary
E4D/E5	32°05.5′–32°23.0′ (minimum)	R	16.7	32.8 (minimum)	OSC (deep overlap basin)

[14] Segment W3 (Figure 4) includes the shallowest (<2100 m) and most inflated (~9 km^2, following the *Scheirer and Macdonald* [1993] technique) parts of the axes we investigated, at an eruptive center near 27°44′S, 112°55′W [*Martinez et al.*, 1997]. Northern and southern rift zones extending away from this volcanic center define subsegment W3A, with an average trend of ~N06°W (Figure 4). At the northern tip of the northern rift zone there have been a sequence of "self-decapitation" propagation events [*Macdonald et al.*, 1987]. The axial ridge closest to W2 appears to be the most recently active and is the most strongly rotated toward it, although the sequence of abandoned tips does not show much curvature. The shallow bathymetry extending almost to 27°30′S probably indicates the previous northern extent of segment W3A.

[15] The W3A/3B discontinuity, near 27°56.5′S, is a 2 km right-stepping mismatch of volcanic rift zones, with little or no overlap, a small nonoverlapping offset (SNOO) in the terminology of *Batiza and Margolis* [1986], probably a third-order discontinuity in the terminology of *Macdonald et al.* [1991] and *White et al.* [2000]. W3B has a separate volcanic center near 27°59′S, and is shorter and deeper than W3A, with north and south rift zones both trending ~N08°W. The W3B/3C right-stepping discontinuity, near 28°04′S, may be a very small OSC, with offset width and length both ~1 km. It results from nonintersecting rift zones, with different azimuths, and there is essentially no overlap basin.

[16] W3C has a significantly different azimuth, N01°W, over most of its length. It plunges south from its shallowest point, ~2175 m, at the W3B/3C offset. There are either small discontinuities or jogs in the axis near 28°13′S and 28°15′S, and the inflation profile (Figure 2) suggests a possible discontinuity near 28°12′S.

[17] The right-stepping W3/W4 discontinuity is a classic OSC nontransform offset. The rift zone offset width is ~6 km and the overlap length is ~21 km, and there is a 500 m deep overlap basin (Figures 4 and 5;Table 1).

[18] Segment W4 (Figure 5) forms the western margin of what appears to be a giant (>10,000 km^2) overlap zone formed by the present large-scale dueling propagation [*Hey et al.*, 1995]. This is consistent with the seismicity pattern, which shows distributed bookshelf-type faulting in this zone [*Wetzel et al.*, 1993]. Figure 5 suggests W4 consists of three major subsegments, but our hydrothermal results suggest not all may be actively spreading today.

[19] The northernmost subsegment, W4A, is shallow, inflated, and hydrothermally active, and we are confident that active spreading occurs along its length. Rift zones extend north and south from an

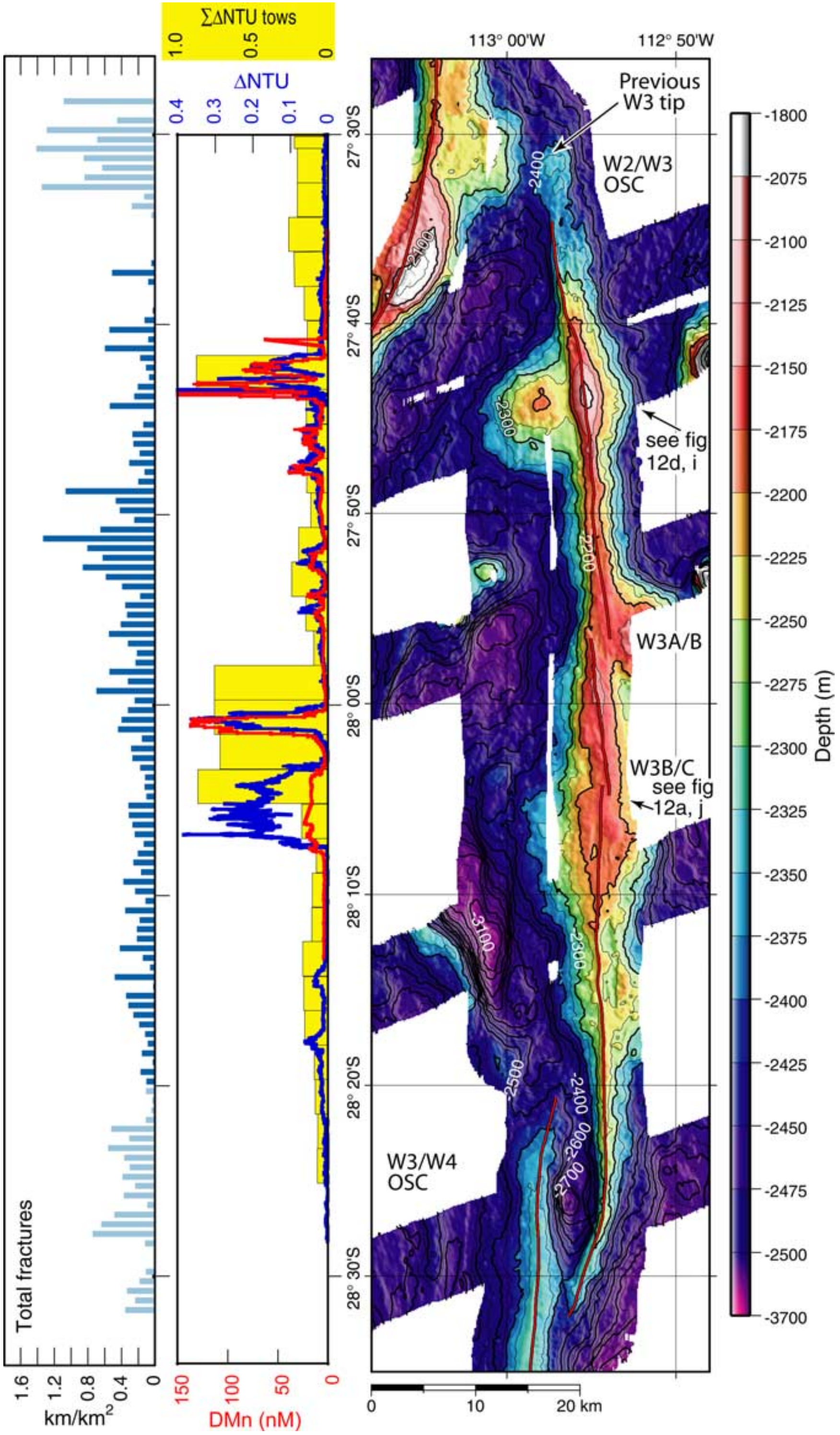

Figure 4. Segment W3 SeaBeam bathymetry, using color scale optimized to show local axial pattern. Far left panel shows total fractures digitized from DSL-120 side-scan data, left panel shows along-axis variability in DMn (red) and ΔNTU (blue) from the side-scan-mounted SUAVE, and vertically integrated ΔNTU (yellow) in 0.03° bins from the CTDO tow-yos (see Figure 10 as well). Locations of Figures 12a, 12d, 12i, and 12j data are shown.

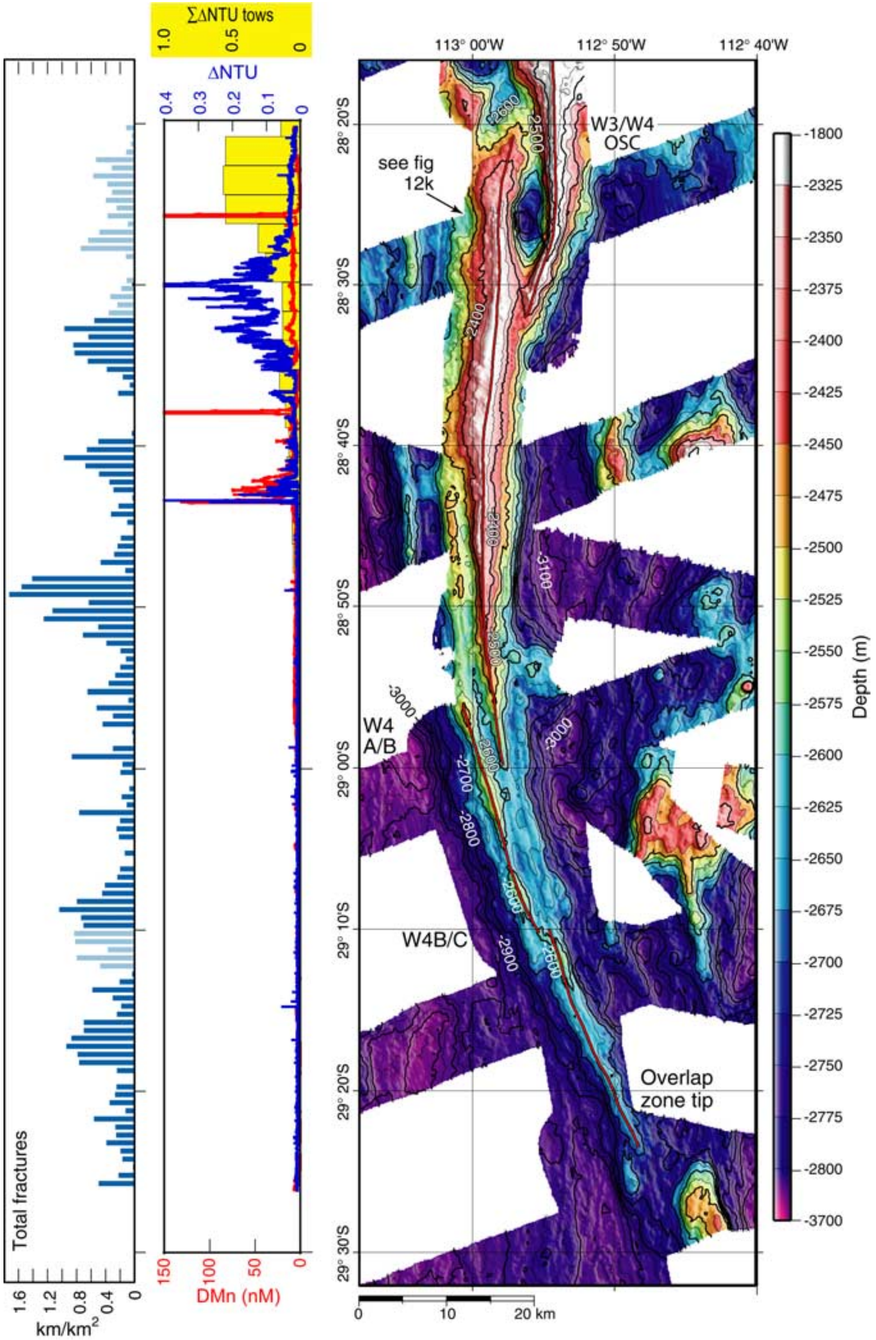

Figure 5. Segment W4 SeaBeam bathymetry, using color scale optimized to show local axial pattern. Far left panel shows total fractures digitized from DSL-120 side-scan data, left panel shows along-axis variability in DMn (red) and ΔNTU (blue) from the side-scan-mounted SUAVE, and vertically integrated ΔNTU (yellow) in 0.03° bins from the CTDO tow-yos (see Figure 10 as well). Compare the plume results from the east limb of the overlapper (Figure 4) with the west limb here. Location of Figure 12k data is shown.

elongate volcano centered near 28°34′S. The northern rift zone, with an azimuth of ~N07°E (except near the OSC), forms the OSC with W3. The southern rift zone trends ~N01°E over most of its length and plunges to the south to a tip near 29°S, which may be the active West ridge propagator tip today. This tip gradually curves toward the East ridge, reaching an azimuth of ~N08°W.

However, there is clear bathymetric and side-scan evidence that seafloor spreading has been active much farther south on segments W4B and 4C, which show increasing curvature toward the East ridge system.

[20] The 3 km right-stepping offset between W4A and W4B is consistent with very recent spreading cessation on W4B, with the abandoned ridge displaced west relative to W4A by renewed spreading on the dueling segment E1. W4B, which shows an overall plunge from north to south and trends ~N17°W, includes three separate volcanic centers spaced about 11 km apart, suggesting that along-strike magmatic connectivity is lost during rift failure. This is consistent with observations at the Galapagos 95.5°W area, where a sequence of failed rift grabens shows that rift failure is less continuous than rift propagation [*Hey et al.*, 1986; *Kleinrock et al.*, 1989]. This subsegment is now being replaced by W4A cutting inside it. Near 29°10′S there is a ~1 km left-stepping offset to subsegment W4C. These appear to be nonintersecting rift zones with no obvious overlap, although the axial locations are uncertain.

[21] W4C trends ~N26°W and also generally plunges to the south, and there are several much smaller scale discontinuities along it, with several local volcanic highs. Subsegment definitions in such areas become somewhat arbitrary. The tip of W4C, near 29°24′S, is of interest because the SeaBeam bathymetry (Figures 2 and 5) and GLORIA side scan [*Hey et al.*, 1995] show it is surrounded by older seafloor and thus marks the southernmost point yet reached by the southward propagating West ridge. Although there has clearly been recent seafloor spreading on W4C and W4B, there may not be active spreading at present. Certainly there is a distinct lack of hydrothermal activity relative to the other West ridge segments [*Baker et al.*, 2002]. The southernmost region of acoustically dark flows thought to show recent fissure eruptions seen in our DSL-120 side-scan data is near 28°46′S on subsegment W4A.

3.2. East Ridge

[22] Segment E1 (Figure 6) was created by the very recent episode of dueling northward propagation of the East ridge, and forms the eastern boundary of the overlap zone (Figure 1). It plunges from its shallowest point at the E1/E2 discontinuity (2475 m) north to ~2725 m at its tip, an average slope of ~0.1°, and the axial inflation shows a similar plunge (Figure 3). There appear to be several E1 subsegments, each defined by separate elongate axial volcanoes, with the discontinuities separating these subsegments occurring where the respective rift zones fail to intersect exactly (Table 1). This segmentation definition is somewhat arbitrary because these five major subsegments change trend at several “devals” [*Langmuir et al.*, 1986] and are offset slightly at several SNOOS and thus are further segmented along axis at a scale of a few km. The axial azimuth curves systematically from N28°W on E1A to about N-S on E1D and N07°E on the southern part of E1E. Whether or not the northernmost subsegment, E1A, is presently active is unknown, but evidence from GLORIA side scan for recent volcanism and NW-trending structures cutting across older seafloor fabric rotated by the dueling propagating rift tectonics show that E1A has been volcanically and tectonically active to ~28°40′S until very recently [*Hey et al.*, 1995]. However E1A, as well as most of E1, is hydrothermally inactive [*Baker et al.*, 2002]. The northernmost occurrence of young dark flows in the DSL-120 side-scan data, which we think show recent sheet-flow eruptions, is from a fissure near the top of the axial ridge near 29°06′S on subsegment E1B. The most robust subsegment, E1E, may be replacing subsegments farther north.

[23] The E1/E2 discontinuity is a small left-stepping OSC (Figures 6 and 7). It is presently located near 30°08′S, although it has varied in the recent past from 30°03′S to 30°15′S. There is evidence for several northward self-decapitation propagation events on E2 that have left abandoned ridges on the Nazca plate, as well as lava flows from the different tips of E2. The present overlap width is ~3 km, with an overlap length of ~4 km. There may be a tiny overlap basin, but the overlap zone is basically a broad high. The shallowest part of E1 occurs here, but not E2, which is ~100 m shallower than E1 and plunges northward toward this discontinuity. There is very slight curvature of the axes toward each other. This area shares elements of a Lonsdale-type OSC, in which nonintersecting rift zones extend from a volcanic center, similar to the Kilauea caldera geometry on the Big Island of Hawaii, and a Macdonald-type OSC, in which there is nonintersection of rift zones at their distal ends, far from the volcanic centers.

[24] Segment E2 (Figure 7) is essentially one long linear volcano with colinear rift zones trending ~N09°E. There may be a very small right-stepping offset between rift zones at 30°20′S, with the southern subsegment shallower and more

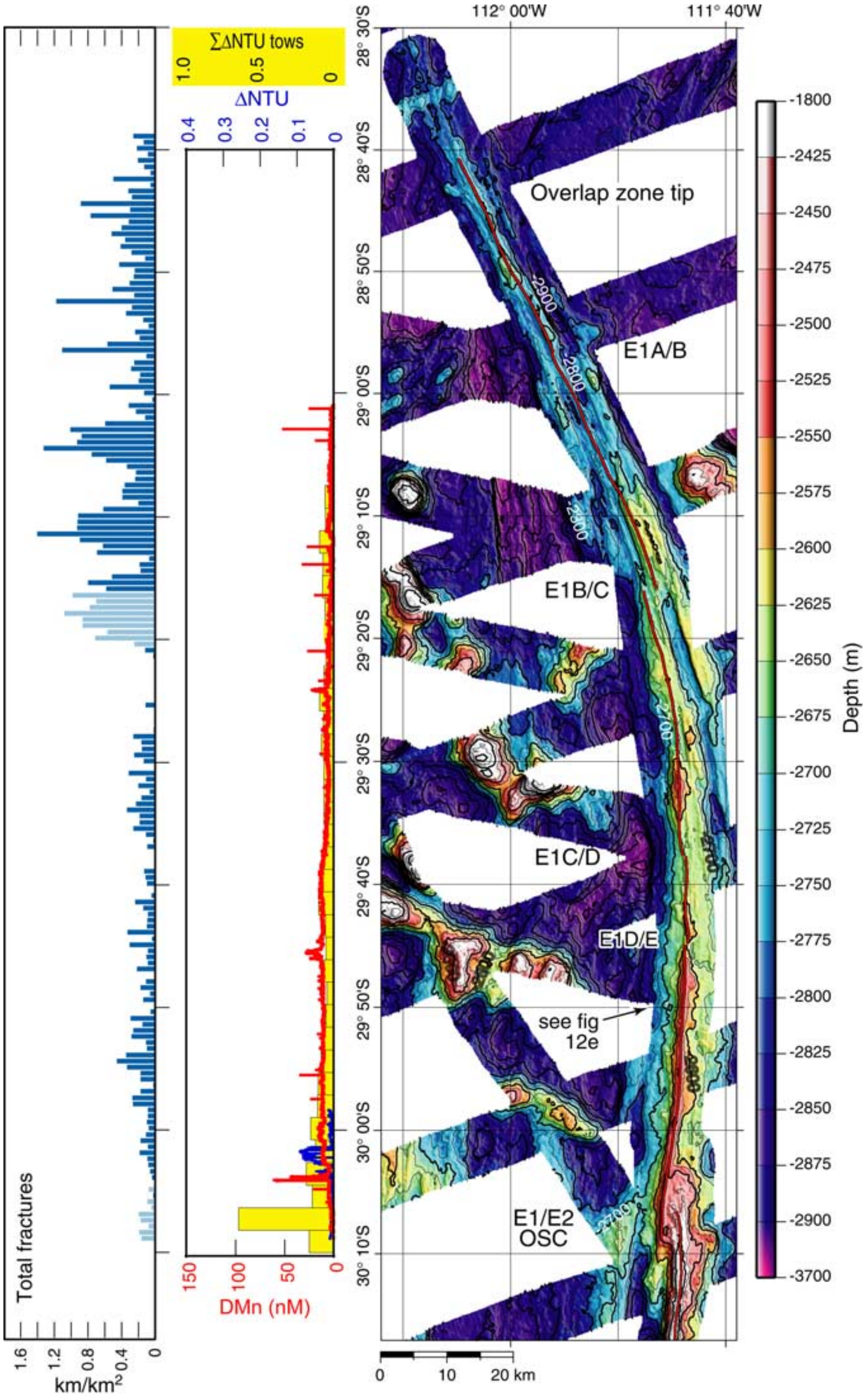

Figure 6. Segment E1 SeaBeam bathymetry, using color scale optimized to show local axial pattern. Far left panel shows total fractures digitized from DSL-120 side-scan data, left panel shows along-axis variability in DMn (red) and ΔNTU (blue) from the side-scan-mounted SUAVE, and vertically integrated ΔNTU (yellow) in 0.03° bins from the CTDO tow-yos (see Figure 11 as well). The SUAVE optical sensor was inoperative for most of this tow. Locations of Figures 12e and 12f data are shown.

inflated. E2 is about 63 km long, with a depth of 2350 ± 50 m along most of its length. Ridges with this kind of V-shaped (low-inflation) profile (Figure 3) elsewhere on the EPR correlate with a lack of axial magma chambers [*Macdonald and Fox*, 1988]. E2 shows low hydrothermal activity relative to other axes with similar depths [*Baker et al.*, 2002].

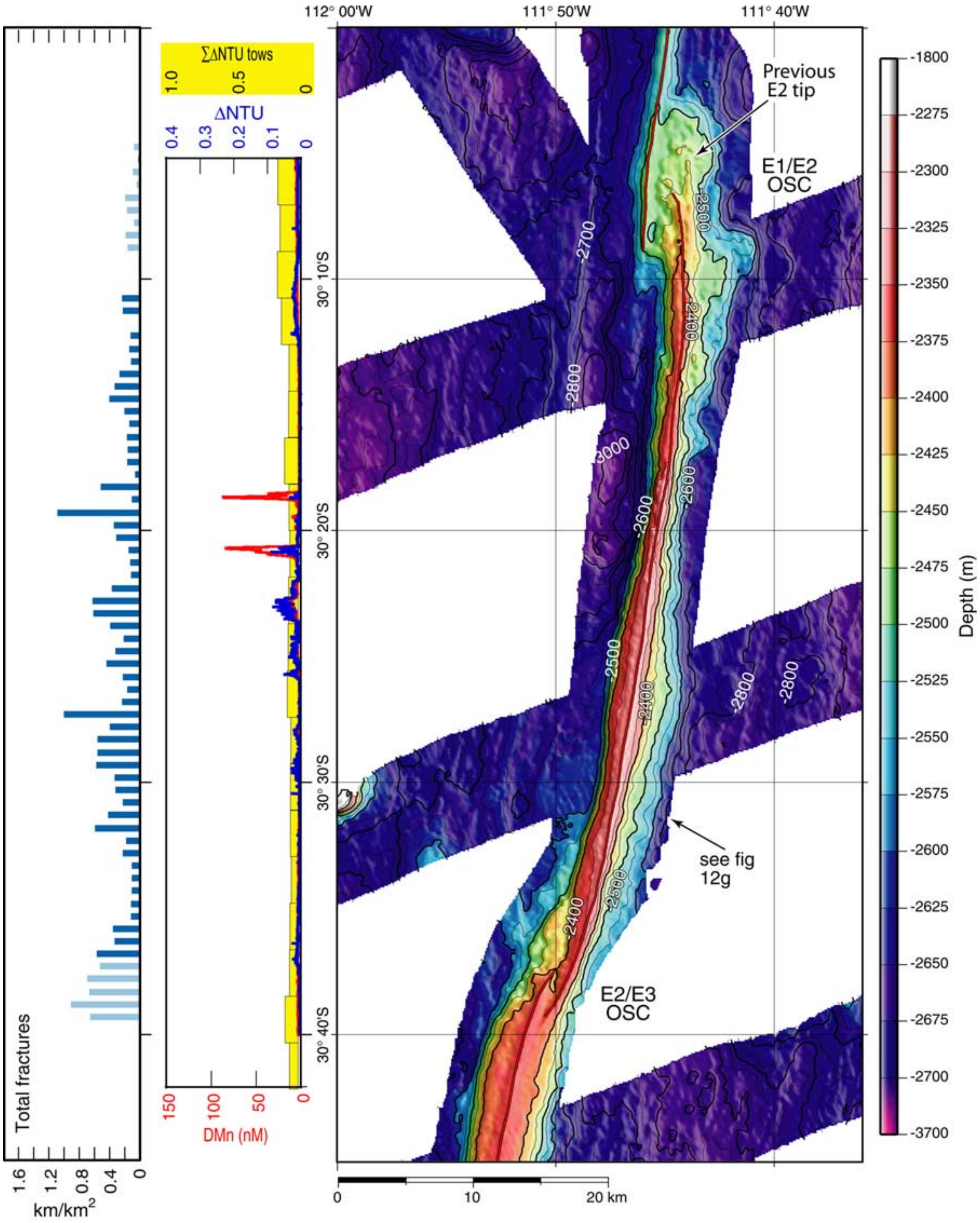

Figure 7. Segment E2 SeaBeam bathymetry, using color scale optimized to show local axial pattern. Far left panel shows total fractures digitized from DSL-120 side-scan data, left panel shows along-axis variability in DMn (red) and ΔNTU (blue) from the side-scan-mounted SUAVE, and vertically integrated ΔNTU (yellow) in 0.03° bins from the CTDO tow-yos (see Figure 11 as well). Locations of Figures 12g and 12h data are shown.

[25] The E2/E3 discontinuity (Figures 7 and 8) is a right-stepping OSC near 30°38′S. The offset width is ~1 km, and the overlap length is ~3 km. There may be a very small (25 m) overlap basin, or this could just be a ridge flank caught between two overlapping rift zones. E2 is slightly shallower than

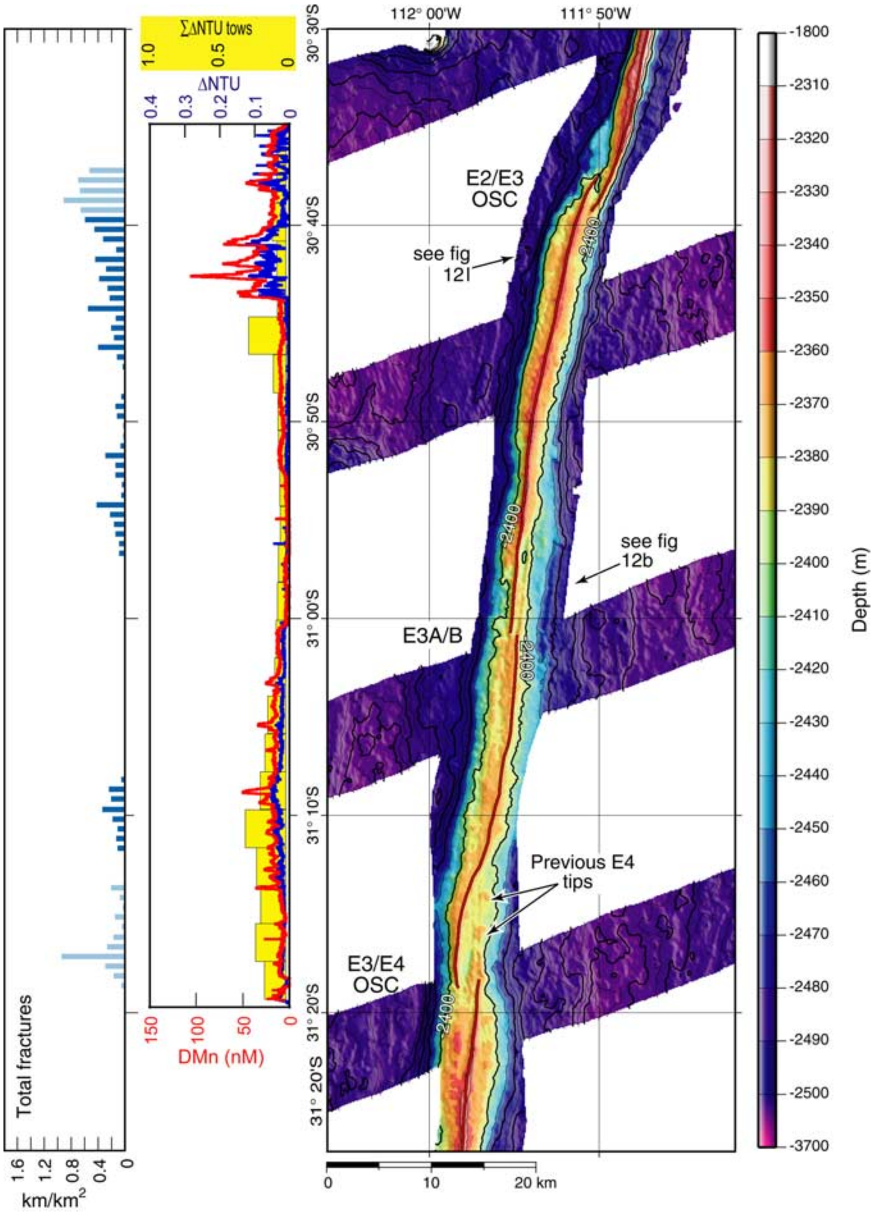

Figure 8. Segment E3 SeaBeam bathymetry, using color scale optimized to show local axial pattern. Far left panel shows total fractures digitized from DSL-120 side-scan data, left panel shows along-axis variability in DMn (red) and ΔNTU (blue) from the side-scan-mounted SUAVE, and vertically integrated ΔNTU (yellow) in 0.03° bins from the CTDO tow-yos (see Figure 11 as well). Locations of Figures 12b and 12l data are shown.

E3 near the offset, 2320 m versus 2350 m, but E3 is much broader and more inflated (Figure 3).

[26] Segment E3 (Figure 8) is about 81 km long. There are two major volcanic centers, one near 30°50′S and the other near 31°06′S. Their rift zones have a small mismatch near 31°01′S, a left-stepping 0.6 km offset, separating subsegments 3A and 3B. E3A is systematically shallower than E3B, 2350 m versus 2370 m, but the entire segment has a very constant ridge elevation and an average trend of ~N06°E except approaching the bounding OSCs. E3A appears to be lengthening at the expense of E3B, leaving a possible abandoned ridge on the Nazca plate near 31°S.

[27] The E3/E4 discontinuity (Figures 8 and 9) is another nontransform offset, a left-stepping OSC near 31°18′S. Its offset width is ~2 km and its overlap length is ~1 km, although it was longer recently. There may have been recent propagation of E3 to the south, as there appear to be abandoned

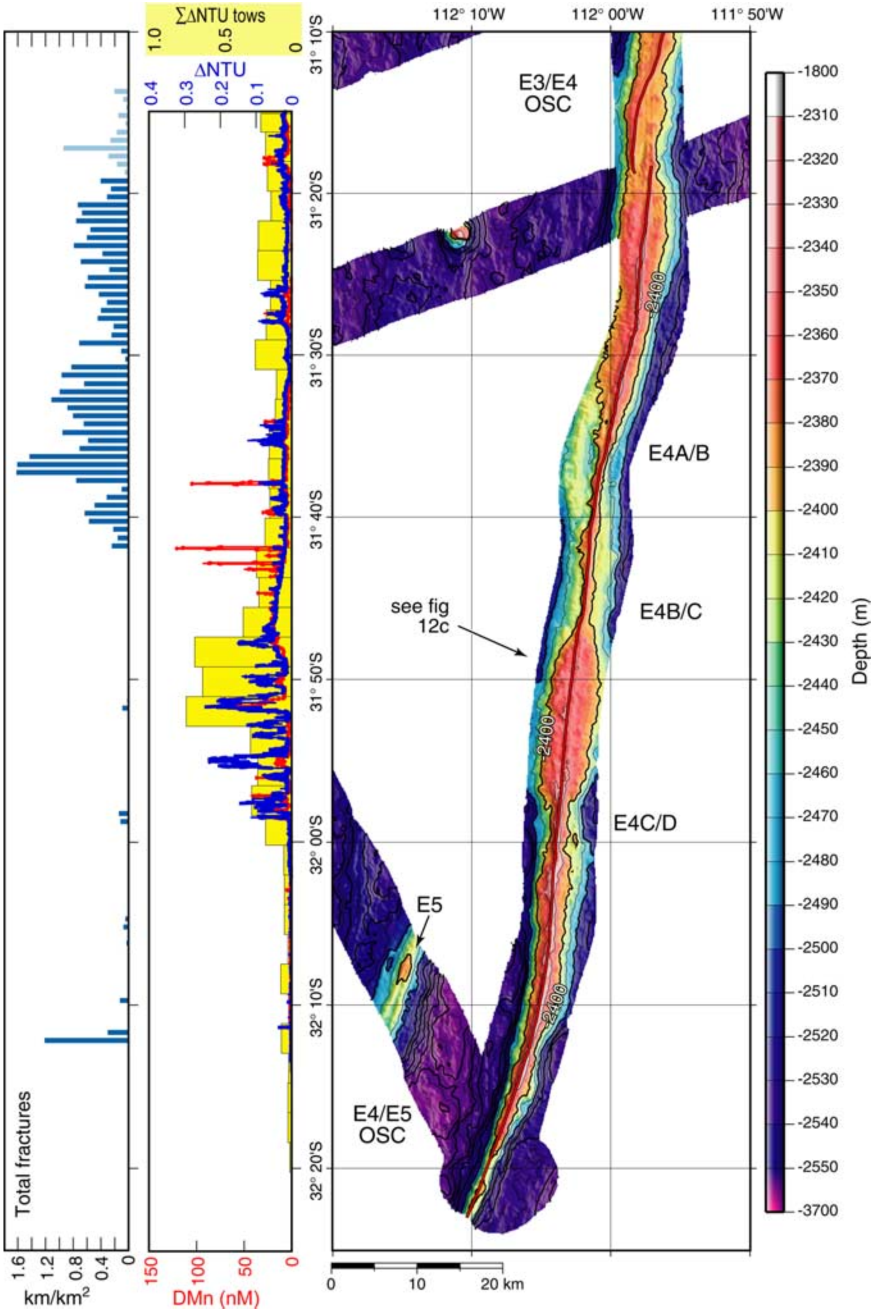

Figure 9. Segment E4 SeaBeam bathymetry, using color scale optimized to show local axial pattern. Far left panel shows total fractures digitized from DSL-120 side-scan data, left panel shows along-axis variability in DMn (red) and ΔNTU (blue) from the side-scan-mounted SUAVE, and vertically integrated ΔNTU (yellow) in 0.03° bins from the CTDO tow-yos (see Figure 11 as well). Location of Figure 12c data is shown.

ridge tips on the Nazca plate extending north away from this OSC. E3 shows curvature first away and then toward E4, similar to the geometry analyzed by *Pollard and Aydin* [1984] and *Sempere and Macdonald* [1986] in terms of overlapping interacting cracks. E3 and E4 were nearly colinear in the recent past before this discontinuity grew. The fastest active seafloor spreading is predicted to occur just north of the Juan Fernandez microplate, probably on segment E3 or E4 (the northern microplate boundary is somewhat diffuse). To the south, total Pacific-Nazca opening continues to increase [e.g., *DeMets et al.*, 1990, 1994; *Naar and Hey*, 1989b], but some of this opening is taken up on the eastern Juan Fernandez microplate boundary [*Anderson-Fontana et al.*, 1986; *Larson et al.*, 1992; *Bird et al.*, 1998].

[28] Segment E4 (Figure 9) has about the same depth as E3, ~2375 m, but is much more inflated (Figure 3) [*Martinez et al.*, 1997]. Its minimum length is 125 km. It shows several subsegments defined by changes in azimuth and sometimes by discontinuities in the axial inflation pattern. Segment E4A has a N-S oriented volcanic center with two rift zones extending away at azimuths of about N09°E, forming devals near 31°25 and 31°28′S. This E4A subsegment is highly inflated. Near 31°36′S there is a rapid decrease in inflation to the south, defining subsegment E4B. The inflation remains low until ~31°47′S where it suddenly increases, defining subsegment E4C. There is a sudden increase in hydrothermal activity at the same location, strongly suggesting that inflation is the best hydrothermal predictor on the segment scale [*Baker et al.*, 2002]. Inflation stays high until ~31°58′S where it abruptly decreases, defining subsegment E4D. Segments E4B, C and D are nearly colinear, trending ~N06°E except near the southern tip of E4D where it curves west at a big OSC. There appear to be very small left-stepping offsets near 32°05′ and 32°07′S, and the E4A and 4B rift zones are slightly mismatched near 31°36′S (0.2 km right-stepping offset), but basically these inflation boundaries are not associated with significant axial offsets, suggesting they result from recent magma inflation events that may be migrating along axis. One inflation center is near 31°26′S and the other near 31°53′S, both with depths of ~2350 m. The multibeam data (Figure 9), side-scan data (Figure 12c), and recent ALVIN dives [*Lupton et al.*, 1999; *Won et al.*, 2003] show recent collapse structures associated with strong hydrothermal activity [*Baker et al.*, 2002] along E4C.

[29] E4 ends at the biggest OSC along the East ridge (Figure 9), part of the western boundary of the Juan Fernandez microplate [*Larson et al.*, 1992; *Bird et al.*, 1998]. The offset width is ~17 km, the minimum overlap length is 33 km, and the overlap basin is ~700 m deep. *Bird et al.* [1998] conclude the true overlap length is ~40 km, and that segment E4 has been propagating south.

4. Ridge Segmentation on the DSL-120 Scale

[30] The high-resolution 120 kHz DSL-120 side-scan sonar data show much more detailed patterns of segmentation than the SeaBeam data. Here we discuss the broad tectonic and volcanic segmentation patterns revealed by the side-scan data in relation to the hydrothermal plume distributions mapped by the SUAVE and CTDO operations (Figures 10 and 11). Representative examples of the side-scan data are shown in Figures 12a–12l. Even finer scales of segmentation evident in the side-scan data will be discussed elsewhere (D. R. Bohnenstiehl et al., manuscript in preparation, 2004).

4.1. West Ridge

[31] The plot of total fractures (faults and fissures, including those scarps resulting from linear tectonic collapse) digitized from the side-scan data shows a fundamental scale of segmentation along the West ridge (Figure 10). Three major segments are defined by the fracture pattern, corresponding to segments W3, W4A, and W4B/C, with lengths of ~85 km, ~75 km, and >50 km respectively (part of the W4A/B overlap was not towed). On each of these segments the overall fracture density generally decreases toward the multibeam-defined segment ends, although there are some exceptions and some caveats about these plots.

[32] The major caveat is that the survey tracks can bias these results. For example, the DSL-120 system collects data best in straight lines, so we surveyed the axis along a series of straight-line approximations to the axis, slowly crossing back and forth over it. Sometimes the axis was in the center of the data swath, sometimes near the edge of the swath, occasionally in complex areas slightly outside the data coverage, and near the dueling propagator tips we sometimes do not know exactly where the axis is. Because off-axis areas are older and generally more fractured than on-axis areas, this produced data bias. A good example of this is the peak in fractures near 27°30′S, shown as light stipple in Figure 10, which marks the off-axis data collected during the initial stage of our first DSL-120 tow before reaching the axis.

[33] Another situation in which these data plots can be misleading is in overlap zones such as the W3/W4 OSC near 28°30′S (Figure 10). In situations like these, where we surveyed both limbs of the overlapper, yet plotted the total fractures vs. latitude, the apparent spike in fracture density (shown lighter) is an artifact of summing the two overlapping segments.

[34] Another artifact arises where we continued to tow across a small axial offset to get from one

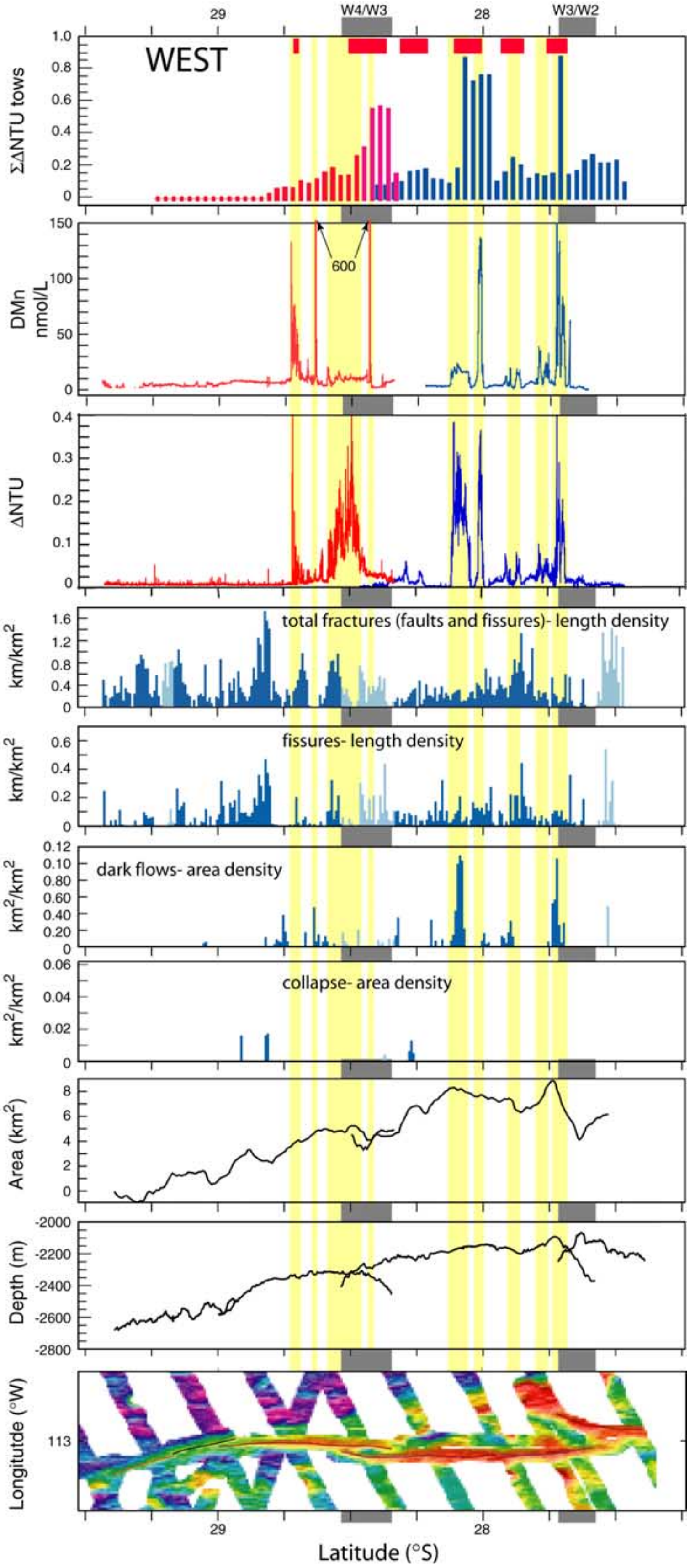
WEST
29
W4/W3
28
W3/W2
ΣΔNTU tows
1.0
0.8
0.6
0.4
0.2
0
DMn nmol/L
150
100
50
0
600
ΔNTU
0.4
0.3
0.2
0.1
0
km/km²
total fractures (faults and fissures)- length density
1.6
1.2
0.8
0.4
0
fissures- length density
0.6
0.4
0.2
0
km²/km²
dark flows- area density
0.12
0.10
0.80
0.60
0.40
0.20
0
collapse- area density
0.06
0.04
0.02
0
Area (km²)
8
6
4
2
0
Depth (m)
-2000
-2200
-2400
-2600
-2800
Longitude (°W)
113
Latitude (°S)

Figure 10

subsegment axis to another, with the more intensely fractured off-axis data producing an apparent spike in the data that is not indicative of the axial pattern. For example, the off-axis transit from W4B to W4C explains the data peak near 29°10′S. Thus local minima in these plots are considered more fundamental than local maxima, with some minima created instantaneously by eruptions burying all fractures.

[35] Despite these problems, there are robust data patterns that define a structural scale of segmentation. On W3, there is a systematic large-scale fracture pattern, with a peak near 27°52′S along the southern rift zone of the northernmost volcanic center. There are fractured areas near the segment ends, but the overall pattern shows that fracturing generally decreases toward the segment ends.

[36] W4A shows a broad pattern of intense fracturing in the south, generally decreasing toward the north, but with young eruptive areas of volcano-constructional terrain overwriting this overall pattern. The local low in total fractures just north of 28°40′S is an area of young constructional volcanism which has buried the tectonic structures. This probably marks the major eruptive center along this axis, although it could occur slightly farther north, just south of 28°30′S, where the fracture minimum also marks young resurfaced volcano-constructional terrain. These areas have recently erupted along what appears to have been a heavily fractured area centered along the dominant magmatic center of W4A.

[37] The southernmost present active spreading along the West ridge may occur along segment W4A. Although there was clearly previous spreading on both W4B and W4C, these may have been such brief episodes that these axes could be combination fossil ridges and pseudofaults from the initial stages of propagation that reached that far south. Thus the southern tip of W4A, near 29°S, may mark the active propagator tip today. There is a marked drop in hydrothermal activity near 28°42′S, and there is no hydrothermal signal south of 29°S on W4B or W4C (Figure 10) [*Baker et al.*, 2002].

4.2. East Ridge

[38] The fault and fissure patterns in the side-scan data also appear to define a fundamental scale of axial segmentation on the East ridge system (Figure 11) that differs somewhat from that inferred from the multibeam data. The major segments defined by the fracture pattern correspond to segments E1A/B, E1C/E, E2, E3, E4A/B, and E4C/D, with lengths of ~70 km, ~90 km, ~60 km, ~70 km, ~50 km, and >60 km, respectively (weather prevented us from reaching the southern tip of E4).

[39] On segment E1, the fault and fissure pattern (Figure 11) suggests the major discontinuity between the five major subsegments occurs near 29°24′S. However, the densely faulted and fissured area shown in light stipple near 29°20′S is an artifact of our survey track in this area, which was temporarily off-axis while we were transiting from the E1C axis to the E1B axis. If we had stayed on the much less fissured E1C axis, we suspect the sparsely fractured pattern would have extended to near the E1C/E1B offset near 29°16′S, which we think is probably the northern limit of active seafloor spreading today. To the north, the bathymetric ridge is displaced 3 km to the east. If this displacement resulted from seafloor spreading on the West ridge following (temporary?) cessation of spreading here, it would suggest E1A and E1B stopped spreading ~20 kyr ago. Farther north the seafloor is extensively fractured, and there is no hydrothermal signal north of 29°09′S.

[40] There are some significant differences seen in the along-segment fault and fissure patterns. For example, E2 shows a maximum density of fractures near the segment center, generally decreasing toward the segment ends, except for a short densely faulted and fissured area at the E2/E3 OSC. E3 shows the opposite pattern, with a minimum in faults and fissures near the segment center, with fracture density increasing toward the segment ends. The fracture density along E1C/E is uni-

Figure 10. West ridge summary plot of hydrothermal and geological patterns. $\sum\Delta$NTU data were collected during CTDO tow-yos. DMn and ΔNTU data were collected with the SUAVE chemical analyzer mounted on the DSL-120 sled. Alternating colors show different segment tows. Dark flows, collapse structures, faults, and fissures were digitized from the DSL-120 side-scan data. Light areas in these plots show artifactual areas as discussed in text. Second-order segment boundaries defined by SeaBeam bathymetry shown as gray stripes. Yellow bands indicate hydrothermally active areas based on SUAVE data where DMn > 15 nmol/L and/or ΔNTU > 0.05. These areas generally agree with vent field locations identified using CTDO hydrographic and chemical anomalies [*Baker et al.*, 2002], shown as red stripes in the top panel.

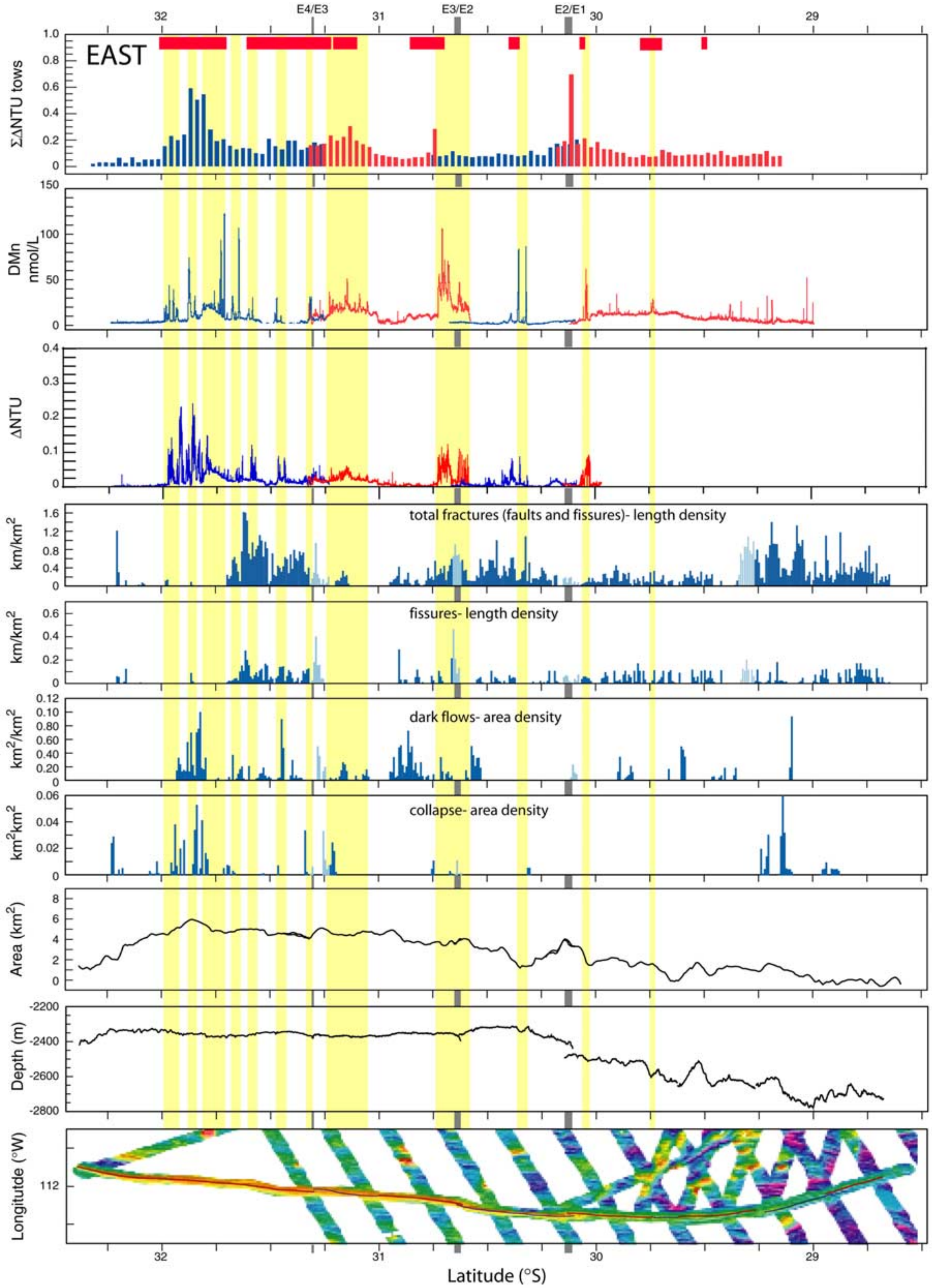
EAST
E4/E3
E3/E2
E2/E1
32
31
30
29
ΣΔNTU tows
DMn nmol/L
ΔNTU
total fractures (faults and fissures)- length density
km/km2
fissures- length density
dark flows- area density
km2/km2
collapse- area density
Area (km2)
Depth (m)
Longitude (°W)
112
Latitude (°S)

Figure 11

formly low. E4 is heavily fractured north of ~31°40′S, whereas a recent eruption to the south has buried almost all of the tectonic structures.

[41] The fracture patterns observed in the side-scan data suggest that some subsegments are behaving cohesively, with in-phase tectonic activity, while there are fundamental discontinuities between other subsegments. The combination of East and West ridge data suggests a characteristic structural wavelength here of ~70 km ± 20 km. This structural scale of segmentation usually ignores the principal volcanic centers, as well as most of the subsegment boundaries (these would be third-order discontinuities following *White et al.* [2000] and *Macdonald et al.* [1991]). This indicates the plate boundary fracturing is caused by larger-scale processes than those producing the third-order segmentation, thought to represent individual volcanoes [*White et al.*, 2000]. The surficial fracture patterns must also reflect different processes than the larger-scale segmentation presumably resulting from deeper crustal and mantle processes, because the multibeam-defined (second-order) segments range in length from ~60–170 km. Assuming a decadal eruption frequency at these spreading rates (based on 1 m wide dikes and a 0.15 m/yr spreading rate), following volcanic resurfacing events these faults and fissures must develop very rapidly due to stretching caused by plate motions or the inflation [e.g., *Bohnenstiehl and Carbotte*, 2001] and deflation [e.g., *Carbotte et al.*, 2003] of the axial region.

[42] In addition to the faults and fissures, there are several distinctive classes of volcanic features that were also digitized to test for correlations with the hydrothermal pattern (Figures 10 and 11). These include acoustically low backscatter (dark) flows (Figure 12a), acoustically high backscatter (light) flows (Figure 12b), and collapse structures (Figure 12c). These correlations suggest that fissures or major collapse areas with voluminous dark flows are areas of recent seafloor eruptions (Figures 12a, 12c, and 12d).

[43] Many dark flows extend several hundred meters (some at least 500 m) downhill out of axial fissures (Figure 12a), and some have built levees, suggesting some combination of relatively low viscosity and high effusion rates [e.g., *Griffiths and Fink*, 1992; *Gregg and Fornari*, 1998; *Chadwick et al.*, 2001; *Cormier et al.*, 2003]. The relative darkness of these flows indicates relatively low acoustic backscatter, yet morphologically they appear to be the youngest flows in the area, flowing over and around older seafloor, and thus should have the lowest sediment cover and highest backscatter amplitude. To investigate this paradox, we photographed over one dark flow, which appears to be a glassy sheet flow. Acoustic energy hitting these smooth flows may be reflected away from the tow-fish receiver, especially relative to the surrounding rougher terrain, producing the relatively darker images of these flows. The acoustically light flows (Figure 12b), which scatter more acoustic energy than the surrounding seafloor and thus are rougher on the centimeter scale, show little correlation with the hydrothermal pattern. They have pancake shapes and distinct flow fronts, suggesting some combination of relatively high viscosity and low effusion rates, and may be lobate pillow flows.

4.3. Axial Collapse and Graben Structures

[44] There are few well-developed axial summit troughs (AST) [*Fornari et al.*, 2004] along any of the axes, especially along the West ridge. The only possible ASTs along the ~200 km of West ridge axis we surveyed are an ~3 km long graben-like structure near 28°33′S and an ~2 km long structure near 28°47′S. The near complete lack of ASTs could be due to unusually high magma supply throughout this area, particularly along the West ridge system where it is driving the ridge propagation away from the shallowest part of the axis closest to Easter Island.

[45] Along the East ridge there is a linear collapse feature that correlates with the very active northern hydrothermal area on E3 (30°35–46′S). Major irregular volcanic collapse areas are also observed along the highly inflated part of this axis between ~31°48–56′S (Figure 12c). These appear to be in a

Figure 11. East ridge summary plot of hydrothermal and geological patterns. $\sum\Delta$NTU data were collected during CTDO tow-yos. DMn and ΔNTU data were collected with the SUAVE chemical analyzer mounted on the DSL-120 sled. Alternating colors show different segment tows. Dark flows, collapse structures, faults, and fissures were digitized from the DSL-120 side-scan data. Light areas in these plots show artifactual areas as discussed in text. Second-order segment boundaries defined by SeaBeam bathymetry shown as gray stripes. Yellow bands indicate hydrothermally active areas based on SUAVE data where DMn > 15 nmol/L and/or ΔNTU > 0.05. These areas generally agree with vent field locations identified using CTDO hydrographic and chemical anomalies [*Baker et al.*, 2002], shown as red stripes in the top panel.

Fornari et al. [1998] AST stage 1b phase, shortly after a large-volume eruption buried any fissures, but which has already begun to collapse by lava drainback [e.g., *Engels et al.*, 2003]. Some of these collapse areas are found in the largest area of hydrothermal activity (31°42–52′S).

[46] Axial summit graben (ASG), or Stage 4 AST, have been defined more restrictively by *Fornari et al.* [1998] as a pair of antithetic faults that cut the entire brittle layer above the axial magma chamber. Assuming that on-axis faults have near-vertical dips within the upper crust (<400–1000 m below

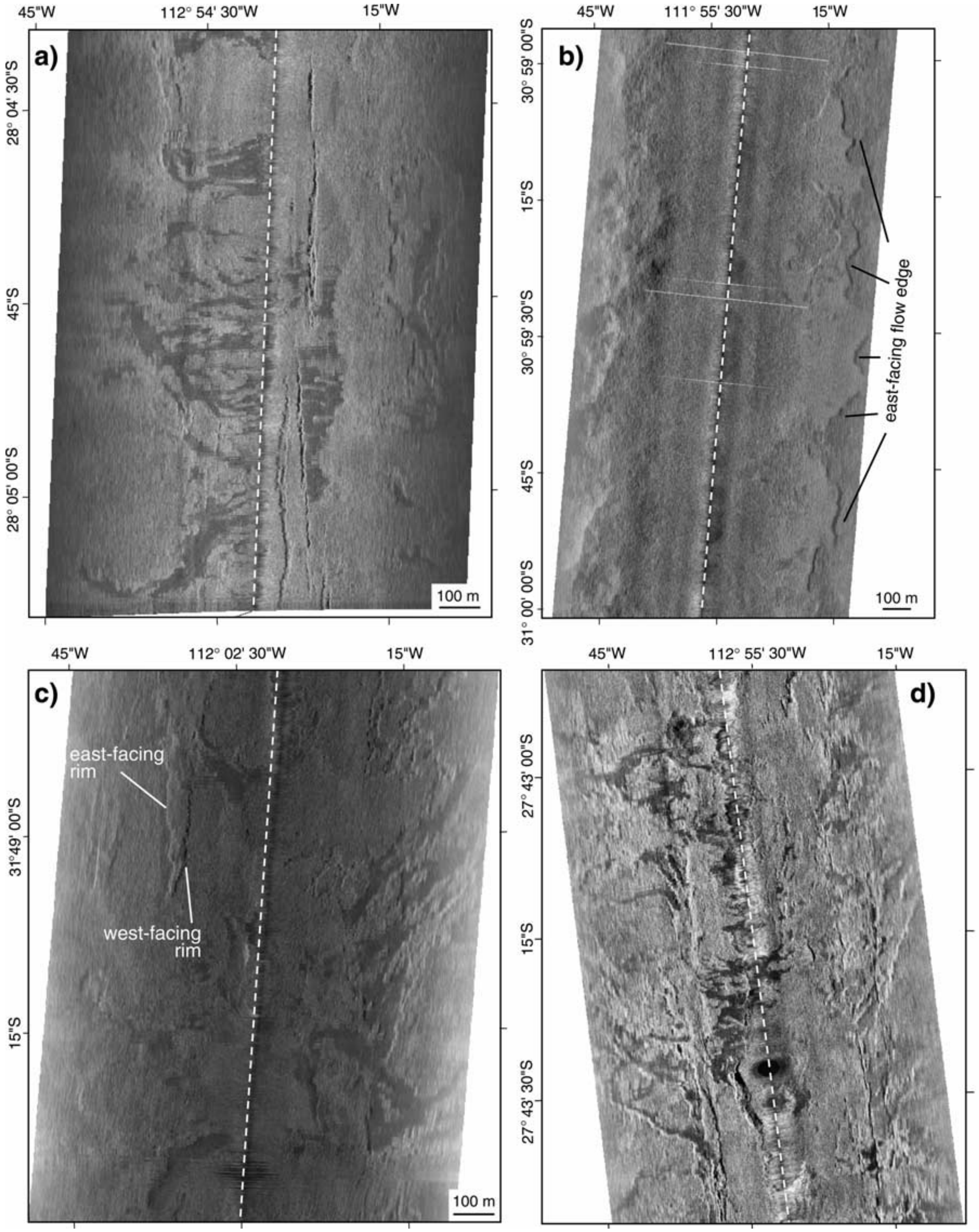

Figure 12

seafloor) and transition at depth to extensional-shear structures with dips of ~70° [see *Bohnenstiehl and Carbotte*, 2001], we limit our definition of ASGs to structures having widths >150 m. Using this criterion, the only ASG in the study area occurs on segment E2, beginning at about 30°22′S, 111°46′W, parallel to and just west of the topographic ridge crest (Figure 12g). The major segment has a fairly constant width of 200–230 m, but ranging up to 300 m, and maximum scarp heights of ~40 m on the east scarp and 30 m on the west scarp (Figure 12h). This feature extends to ~30°33′S, where the western bounding scarp decreases to essentially zero height, ending the graben system. Along this 20 km length of axis, unique along the 600 km of axis we surveyed in having an ASG, there are seven small offsets, one right-stepping and six left-stepping. This ASG occurs on the least-inflated spreading segment we surveyed (other than the dueling propagator tips) and is one of the least hydrothermally active areas. The observation that so little of the ridge is in this ASG stage at present, only about 3%, suggests that eruptions here are generally too frequent to allow this stage to be reached.

5. Hydrothermal Patterns and Correlations

[47] The large-scale pattern of hydrothermal discharge on both ridges was outlined by *Baker et al.* [2002] using data only from the CTDO tow-yos. They identified 14 "vent fields," six on the West ridge and eight on the East (Figures 10 and 11), on the basis of optical, thermal, and chemical plume anomalies. Results from the SUAVE optical and chemical measurements generally agree with this pattern, though the precise location of many of the plumes differs by as much as 10 km. Detailed comparison of the two data sets indicates that plume advection by local bottom currents can account for this difference [*Walker et al.*, 2004]. Without knowledge of the actual locations of the vent fields it is impossible to know which data set is more correct; likely both sets have strengths and weaknesses. We suspect, however, that SUAVE, continually recording chemical and optical anomalies only 100 mab, may prove a more accurate locator of discharge sites than the CTDO tow-yos.

5.1. West Ridge

[48] Both the integrated ($\sum\Delta$NTU) and continuous (DMn and ΔNTU) data identify several plume anomalies along the West ridge that generally match the six vent field areas identified by the CTDO data [*Baker et al.*, 2002] (Figures 4, 5, and 10). The value of multiple sensors that can track both particulate and dissolved hydrothermal tracers is demonstrated by the contrasting characteristics of the plumes centered near 28°30′ and 28°42′S: the former is most clearly defined by ΔNTU, and the latter by DMn (Figure 10).

[49] The two most intense plume centers on Segment W3, at 27°42′ and 28°04′S, both correlate closely with inflation peaks (>8 km^2) that exceed those anywhere else in the study area (and even the weak plumes at 27°53′ and 28°12–20′S correspond to minor inflation peaks). The 27°42′S area, technically part of the W2/W3 overlap (Figure 4), is recently resurfaced by volcanic flows, with a single well-defined fissure, the northernmost such terrain seen on the West ridge (Figure 12i). Some acoustically dark flows come from this fissure, and voluminous dark sheet flows also occur slightly south, from 27°43–44′S (Figure 12d). The 28°04′S area, on subsegment W3A (Figure 4), appears from the SUAVE hydrothermal sensors to contain at least two distinct vent fields, centered near 28°02′S and 28°06′S. The acoustic imagery of the

Figure 12. Figures 12a–12d show DSL-120 side-scan sonar images, each 1 km wide with dashed line showing nadir along instrument tow path: (a) fissures and acoustically dark flows, (b) acoustically light flows, (c) collapse structures and dark flows, and (d) recent eruptive area, including dark flows. Locations of these data examples are noted in Figures 4, 8, and 9. Figures 12e–12h show DSL-120 side-scan sonar images, with exceptions (Figures 12f and 12h) noted: (e) single fissure in volcanically resurfaced area, (f) photograph (~3 × 5 m) of vent biology from fissure vent site shown in Figure 12e), including anemones, bivalves, and tubeworms, (g) overlapping ASG (AST stage 4) segments, and (h) DSL-120 bathymetry of ASG (AST stage 4) segments shown in Figure 12g), 700 m wide because most of the noisy data along the swath edges has been removed. Locations of these data examples are noted in Figures 6 and 7. Figures 12i–12l show DSL-120 side-scan sonar images: (i) area of northernmost intense W3 plume center (Figure 4), single fissure in volcanically resurfaced area with dark flows and constructional volcanic domes, (j) area of southernmost intense W3 plume center (Figure 4), with voluminous dark flows from multiple fissures, (k) area of W4 buoyant plume (Figure 5), in volcanically resurfaced area with two fissures and some constructional domes, and (l) area of northern E3 plume (Figure 8), in zone of developing en echelon right-stepping ASTs. One minute of latitude is one n.m., or 1.852 km.

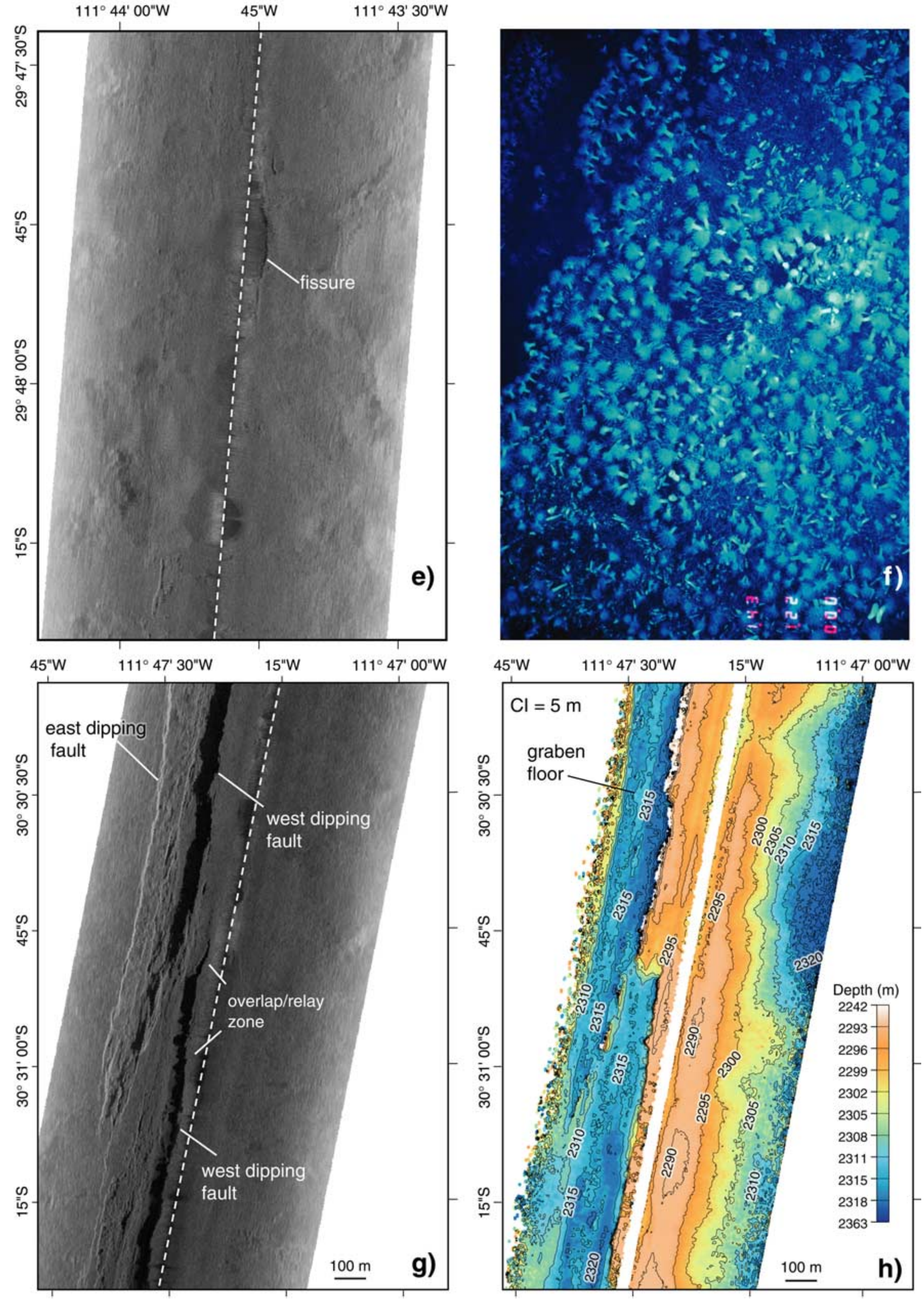

Figure 12. (continued)

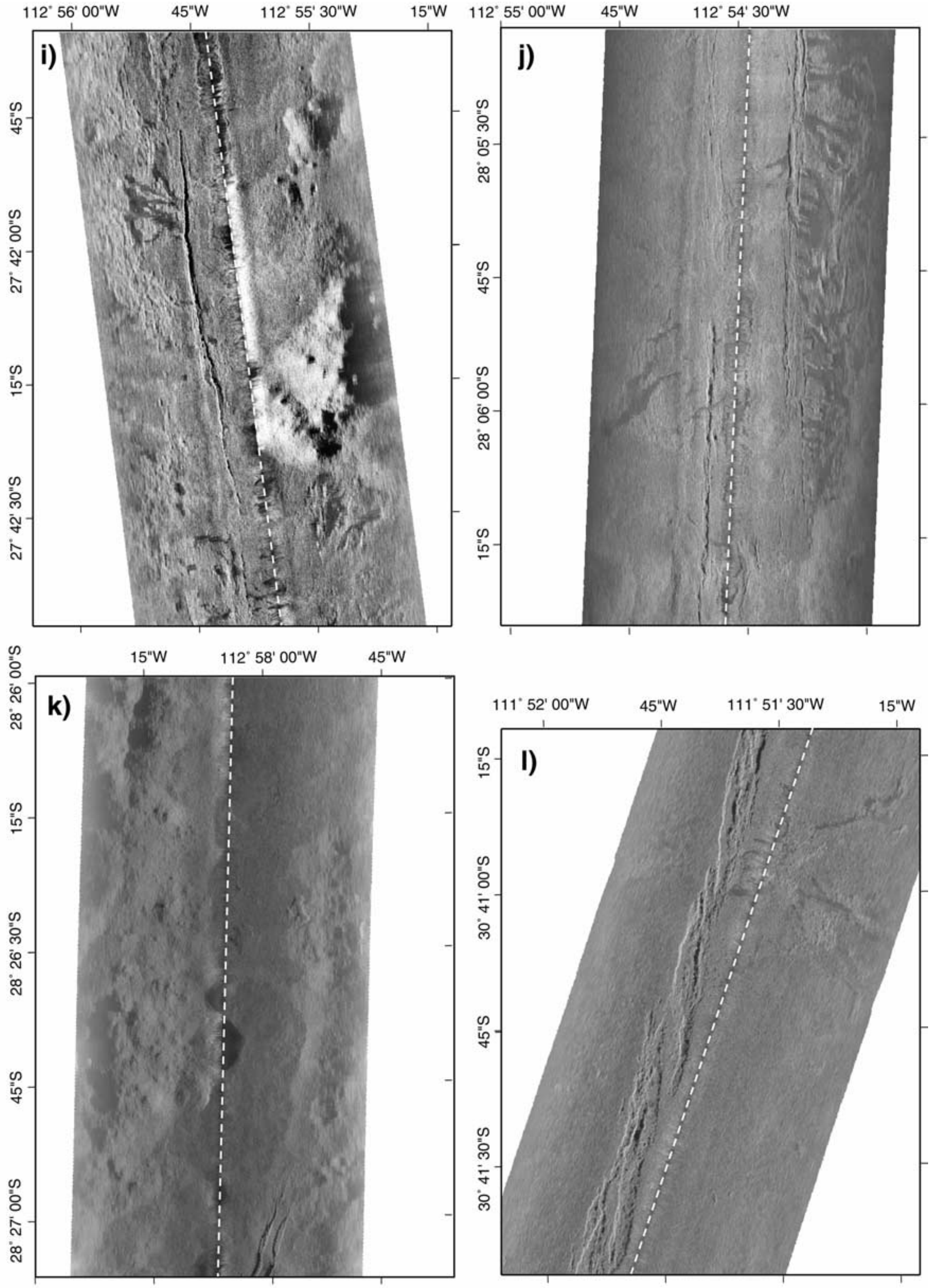

Figure 12. (continued)

28°02′S area is similar to that at 27°42′S, including recent volcanic resurfacing and one dominant deep, wide fissure with a few smaller fissures. The 28°06′S area is broader, and shows voluminous dark flows emanating from multiple fissures (Figure 12j). DMn values in the 28°02′S plume reached a maximum concentration of ∼150 nM, suggestive of high-temperature (>300°C) discharge with high volume flow and an end-member concentration >1 mM [e.g., *Massoth et al.*, 1998]. The SUAVE DMn sensor did not record during passage across the 28°12′–20′S field, but CDTO chemistry data suggest it is a field of low-temperature diffuse flow [*Baker et al.*, 2002].

[50] The major plume on Segment W4 was near its northern end, 28°25–35′S in the SUAVE data and 28°20–30′S in the tow-yo data. This region is within the area of W3/W4 overlap (Figure 5), and has also been recently resurfaced, with only a few fissures (Figure 10). In the tow-yo data, this plume begins near the W3/W4 segment overlap, but evidently originates on W4 where the $\sum\Delta$NTU signal was far higher than on W3 (Figures 4, 5, and 10). This plume was also above a local maximum in axial inflation, especially as located during the DSL-120 tow. The narrow plume at 28°42′S, seen most clearly on the DSL-120 tow, was found over a wide (>1 km) fault and fissure zone. We also encountered two DMn spikes over W4, both of which exceeded 600 nM. We interpret these as patches of perhaps still buoyant, concentrated plumes. The southerly plume, at 28°38′S, was above a recently resurfaced area with no fissures, although several recent flows suggest that a fissure has recently been filled here. The northerly plume, near 28°26′S, is also in a volcanically resurfaced area with a few short fissures (Figure 12k). These two plumes, with no corresponding light scattering signals, surround the only major West ridge hydrothermal area that correlates positively with local peaks in fracture density (Figures 5 and 10). Low temperature fluid discharge can have significant thermal and in some cases chemical (e.g., Mn) flux without producing particle plumes [e.g., *Massoth et al.*, 1998].

5.2. East Ridge

[51] The East ridge hosts centers of hydrothermal activity on every segment, though their extent and intensity vary markedly (Figures 6–9 and 11). The two most northerly on segment E1 (Figures 6 and 11) are both minor: one at 29°30′S is based only on a single water sample (but did occur at a local maximum of axial inflation), but another at 29°45′S was visible as both a weak increase in the SUAVE DMn and as a buoyant plume on the CTDO data [*Baker et al.*, 2002]. A more substantial plume was near the southern end of Segment E1, near the E1/E2 overlap, centered at 30°04′S in the SUAVE data and from 30°03–10′S in the tow-yo data. This area is very young and recently resurfaced, with a single fissure near 30°04′S that cuts through some constructional domes. Many hydrothermal plume areas were found in similar settings (e.g., Figure 12e). Guided by our survey results, we used the WHOI TowCam (http://www.whoi.edu/marops/support_services/list_equip_towed_camera.html) to photograph hydrothermal vent biota at sites on several segments. Typically anemones are the dominant colonizer, although some bivalves and tubeworms are also seen. An example from the 29°45′S E1 vent site is shown in Figure 12f. *Won et al.* [2003] discuss the present biological knowledge of several of the sites.

[52] Other than the tips of the dueling propagator segments, which may not be actively spreading at present, Segment E2 had the lowest plume inventory of any of the surveyed segments. No significant hydrothermal activity can be observed in the integrated tow-yo data, but two hydrothermal spikes were seen in DMn (and small ones in the ΔNTU SUAVE) data near 30°20′S (Figures 7 and 11). The northern spike correlates with a local maximum in fracture density, near the boundary between a broadly fractured area to the south (>500 m wide) and a more focused area of fracturing to the north. A similar change from broader to more focused fracturing occurs at the southern spike near 30°21′S, although here the broader area is only ∼100 m wide. The patterns of shallow depths but low inflation and low hydrothermal activity on segment E2 show that inflation is the better hydrothermal predictor of these parameters [*Baker et al.*, 2002].

[53] South of E2, hydrothermal activity steadily increased, coincident with increasing axial inflation, although the depths are a very constant 2350 ± 25 m. The SUAVE data and tow-yo data both show two centers of activity on Segment E3 (Figures 8 and 11). The northern plume area, including the part of E3 that overlaps with E2, has relatively higher detected DMn values. It occurred from 30°36–44′S in the SUAVE data but 30°44–46′S in the tow-yo data, again suggesting temporal variability in the plume location because of bottom

currents (CTDO and DSL-120 tows here were separated by up to six days [*Walker et al.*, 2004]). This is the only East ridge hydrothermal area that correlates positively with high fracture density. This plume begins at the northern tip of segment E3 (and even slightly beyond, seen for another 3 km as we towed across the overlap basin of the E2/E3 OSC). The seafloor in this area is very young and recently resurfaced, with some collapse structures at its northern end, then a single discrete fissure evolving south into a broad (∼100 m) fissure zone with en echelon right-stepping offsets (Figure 12l), reflecting evolution from stage 1 to stage 2 and 3 AST [*Fornari et al.*, 1998]. We found the strongest DMn signals near 30°40–43′S to coincide with the beginning of the stage 3 AST (although this could be influenced by the distance from our fish track to the axis, as we were slightly off-axis where the ridge axis curves into the OSC). The abrupt end of DSL-120/SUAVE-detected hydrothermal venting near 30°44′S does not correspond to any major change in the volcanic or structural pattern, although it is near a reduction in axial inflation at 30°46′S.

[54] The extensive southern hydrothermal area on E3 begins just south of 31°S, where the hydrothermal signal abruptly increases (Figures 8 and 11). This increase closely corresponds to the beginning of subsegment E3B, which has slightly lower depths but higher inflation than subsegment E3A, again suggesting inflation is the better hydrothermal predictor. The northern part of this area has just been resurfaced, with no fissures but many light flows (e.g., Figure 12b). This southern hydrothermal area on E3 extends to the E3/E4 OSC in both the SUAVE and tow-yo data, where some fissuring occurs. The strongest hydrothermal signal along E3B occurs near 31°08′S in the SUAVE data, and slightly north of this in the tow-yo data. This location closely corresponds to the northernmost fissuring seen on this segment. During a 1999 Vrijenhoek/Lupton Alvin expedition, we explored this area and discovered two separate vent sites, including a high-temperature black smoker and a low-temperature diffuse vent site [*Lupton et al.*, 1999; *Won et al.*, 2003].

[55] Between the end of this site and the beginning of another intense plume center on E4 lies a broad region of slightly elevated ΔNTU and variable chemistry that *Baker et al.* [2002] identified as likely a low-temperature vent field distinct from those immediately to the north and south (Figures 9 and 11). The SUAVE tow found isolated spikes in DMn and ΔNTU in this region, which includes some of most densely fractured axis of the entire survey area (Figure 11).

[56] The most intense and widespread $\sum\Delta$NTU plume on the East ridge, and the highest DMn values, were found along the central part (31°42′–32°S) of segment E4, coincident with the East ridge axial inflation maximum (Figures 9 and 11). The inflation here, using the across-area definition of *Scheirer and Macdonald* [1993], is 5–6 km^2 [*Martinez et al.*, 1997]. This area is virtually devoid of fractures and fissures, but with abundant dark flows and collapse areas (Figure 12c), indicating recent volcanic eruptions.

[57] The higher-resolution SUAVE data show fine-scale plume variability that may reflect variability in the seafloor terrain (Figures 9 and 11). For example, the DMn spike near 31°38′S overlaid a recently resurfaced area with two narrow, discrete fissures ∼300 m apart, near the southern tip of a broader fissure system extending north for ∼40 km. The lack of fissures appears to be the result of recent flows burying most of the fissures, rather than indicating a southward propagating fissure system. A broad DMn high extends from ∼31°41′–31°52′S. The northern part of this area is recently resurfaced, with a single fissure cutting through it, with the southern tip of this fissure near 31°41′S. Just to the south, the area has been so recently resurfaced that no fissures are seen, although minor collapse structures underlie the largest DMn spike (130 nM) on the East ridge (31°41′S). Major collapse structures (Figure 12c) begin near 31°47′S and extend to ∼31°51′S, until an almost buried fissure with voluminous dark sheet flows pouring out of it is seen near 31°52′S, which coincides with strong SUAVE chemical and optical plume signals. We also explored this area on the 1999 Vrijenhoek/Lupton Alvin expedition, and discovered both the low-temperature "Snow Ghosts" vent field and the high-temperature "Saguaro" black smoker vent field [*Lupton et al.*, 1999; *Won et al.*, 2003]. Finally, a lesser area of hydrothermal activity near 31°57′S, in a young resurfaced area with some collapse structures, ends abruptly near a small (∼150 m) axial discontinuity near the southern end of the major inflation peak (Figure 11).

6. Geological Indices of Venting

[58] A primary objective of our surveys was to improve our ability to use geological indices to

predict the location of active venting. Our initial results [*Baker et al.*, 2002] found that the likelihood of observing a significant hydrothermal plume increased linearly with increasing cross-axis inflation, a proxy for the local magmatic budget and heat supply [*Scheirer and Macdonald*, 1993]. This result is confirmed by the inclusion of the SUAVE sensor data (Figures 10 and 11), which in some cases may improve the correspondence between plume location and inflation maxima (e.g., at the north end of W3). This correspondence does not necessarily follow the multibeam subsegment boundaries. In some areas an entire subsegment is locally inflated and overlain by a plume (e.g., E3B and E4C), while in other areas the inflation and plume maxima occupy only a subsegment portion (e.g., W3A, W3C, and W4A).

[59] While a robust correlation exists between inflation and the probability of venting, inflation is not a deterministic indicator. Superfast spreading axial locations where inflation is >6 km^2 have a >80% probability of hosting a hydrothermal plume, but for an inflation of 3–4 km^2 the probability is only ~50% [*Baker et al.*, 2002]. The addition of the side-scan tectonic fabric data markedly improves our ability to identify likely hydrothermal sites. Figures 10 and 11 show that most prominent plumes (yellow bands/red stripes) correlate with local minima in the total fracture length density. The clearest examples are on E3 and E4, where almost no fractures were mapped beneath the major plume centers. The smaller plume at 30°04′–10′S also occurs at a fracture minimum. This anti-correlation is less explicit on the West ridge, but local minima in the fracture density correlate with the major plumes centered at 27°42′ and 28°04′S. The strength of the correlation in the W3/W4 overlap area depends on the actual location of the vent field, since the CTDO and side-scan operations found a difference of >10 km in the plume location.

[60] We interpret these observations as further evidence that the first-order control on the distribution of hydrothermal venting on superfast spreading ridges is the magmatic budget and concomitant heat supply. Even small variations on an axial length scale of tens of kilometers can be correlated with the plume distribution. Ridge sections where the fracture density is low and volcanic flows are obvious identify locations where the most recent eruptions may have paved over the neovolcanic zone, and thus hold the highest likelihood of venting. Our results suggest that the most robust vent search strategy at these spreading rates is to target sites of high inflation, diminished fracture density, and recent volcanic flows, especially those with a single fissure. If the total fracture density is a relative measure of the bulk crustal permeability, then permeability has little control over the location of the most vigorous venting along the axes we surveyed.

7. Discussion

7.1. Comparison With Other Areas

[61] At the 9–10°N EPR vents, the classic fast spreading area for this kind of study, the active vents in the AdVenture field area are located either along the base of the AST walls, or over inferred primary eruptive fissures in the floor of the AST [*Haymon et al.*, 1991, 1993; *Fornari and Embley*, 1995; *Fornari et al.*, 1998, 2004]. In this area the AST is a nearly continuous feature, with near vertical walls, a sinuous shape presumably controlled by surface collapse, and considerable variation in width [*Edwards et al.*, 1991; *Haymon et al.*, 1991; *Fornari et al.*, 1998]. The variations in width correlate with small ridge discontinuities where the AST is discontinuous for short distances or its azimuth changes. Typically the AST in this area is ~70–200 m wide and 8–15 m deep. Interestingly, ASTs of this size are rare along the fastest spreading EPR segments.

[62] A detailed (visual) mapping of cracks and hydrothermal discharge [*Haymon et al.*, 1991, 1993; *Wright et al.*, 1995a, 1995b], in a magmatically robust part of this eruptive area smoothed by fresh lavas that have not yet collapsed, also found a negative correlation between crack density and hydrothermal activity, in agreement with our results. They concluded that the sparse, wide fissures in areas of young lava flows are mainly eruptive (or dike-induced) fissures (in contrast to tectonic fissures which dominate elsewhere), and that most hydrothermal vents occur along these fissures because they can extend deep enough to penetrate the layer 2A/2B boundary and thus tap melt and provide conduits for high-temperature hydrothermal discharge [*Wright et al.*, 1995b]. *Fornari et al.* [2004] concluded that high-temperature vents in this area are found where recent eruptions were focused and drainback of lava into the primary eruptive fissure occurred, with low-temperature venting and biological communities concentrated along this fissure. Studies of smaller axial regions by *Wright et al.* [2002] found a positive correlation between fissure density and

the number of hydrothermal vents near 17°35–40′S, but a negative correlation near 17°25′S, where young flows are presumed to cover fissures. They conclude that most of the fissures in the 17°25′S survey area may be generated by dike intrusions, and that fissuring shows better correlation with second-order than with higher-order segmentation. This contrasts with the EPR 9–10°N area, where fine-scale segment boundaries coincide almost exactly with changes in fissure density and hydrothermal vent abundance [*Haymon et al.*, 1991; *Wright et al.*, 1995a, 1995b]. Our broader scale results at faster spreading rates indicate that while active hydrothermal fields may be found in areas with no to some fractures and fissures, in general venting is most abundant where the fracture/fissure population is sparsest.

[63] *Hooft et al.* [1997] concluded that the intensity of hydrothermal venting along the SEPR correlated poorly with regional variations in both ridge depth and cross-sectional area because hydrothermal activity is closely linked to processes such as diking, eruptions and faulting, which occur on much shorter timescales (∼10–100 years) than the long-term (∼100,000 years) variations in magma supply that determine axial depth and inflation. Although this logic seems sound, *Baker et al.* [1996], *Baker and Urabe* [1996], and *Baker et al.* [2002] found that axial inflation appears to be the best predictor of hydrothermal plume density on the ridge segment and subsegment scale, consistent with our results. *Hooft et al.* [1997] also noted a good correlation between the most hydrothermally active part of the Pacific-Nazca ridge north of the Easter microplate [*Baker and Urabe*, 1996] and areas where *Lonsdale* [1989] found an AST or axial graben in multibeam data (these ∼500 m wide structures are different than anything seen in our survey area). *Hooft et al.* [1997] concluded there is a better correlation between venting and the presence of an AST than with the presence or depth of the magma sill. Although their Figure 11b shows little detailed correlation between venting (light attenuation) and inflation, it shows that all areas of strong hydrothermal activity occur where the ridge cross-sectional area is >3.5 km^2, so in this sense there is a strong positive correlation [*Baker and Urabe*, 1996; *Baker et al.*, 2002]. They also conclude that hydrothermal venting is diffuse where there were recent eruptions, and focused and longer-lived where there is an AST or axial graben, and thus that permeability is a key parameter controlling the localization and longevity of venting.

[64] Our results from 27°–32°S are markedly different, as we found a spatial density of hydrothermal plumes roughly equal to that from 13°30′ to 18°40′S [*Baker and Urabe*, 1996; *Baker et al.*, 2002], over ∼60% of the axis, despite the almost complete absence of ASTs or ASGs. Moreover, the only ASG (AST stage 4) we found in the side-scan data (on segment E2; Figures 12g and 12h) correlates with absence of hydrothermal signal. These results support the hypothesis that magmatic heat is a more important parameter controlling hydrothermal venting than gross permeability of the seafloor in this area, consistent with the interpretations of *Haymon et al.* [1991, 1993], *Haymon* [1996], and *Wright et al.* [1995a, 1995b] at 9–10°N.

[65] One interesting observation that holds for both the East and West ridge systems is that more of the major plume areas are found near segment ends than near segment centers (Figures 4–11). This suggests there is abundant magma being supplied to these areas. This is similar to the pattern near the Azores triple junction, where more hydrothermal sites are found near nontransform offsets than segment centers, although the EPR axes lack the cross-cutting fault fabrics thought to focus the hydrothermal flow along those parts of the slow-spreading Mid-Atlantic Ridge [*German et al.*, 1996].

7.2. Volcanic Domes

[66] *White et al.* [2000, 2002a] concluded that third-order spreading segments, with lengths of ∼20 km and >1 km axial offsets, represent fundamental volcanic units within the fast spreading environment. They suggest that third-order discontinuities correspond to disruptions in the volcanic plumbing system, producing reduced eruption effusion rates and areas of small constructional volcanic domes (see examples in Figures 12i and 12k). Our data partially corroborate the *White et al.* [2000, 2002a] conclusions, except that the only areas of dense domes we observed are at the ends of second-order segments, interpreted here as cohesive volcanic systems with multiple magmatic injection centers. This is more consistent with the 16–19°S region of the EPR, where there are abundant volcanic domes within the off-axis discordant zones of second-order OSCs [*White et al.*, 2002b].

[67] On the West ridge, there are dense areas of domes at both the northern and southern tips of segment W3, but not at the three third-order discontinuities along this segment. There are areas of

domes at the northern and southern tips of segment W4, and one area near the center of segment W4A, but none near a third-order discontinuity.

[68] On the East ridge, what we interpret as the northernmost recently volcanically active axis of segment E1 is an area of many volcanic domes, although the southern tip of segment E1 has only a few domes. One small area of domes is found near the small third-order discontinuity between segments E1A and E1B, and another begins in the middle of segment E1C and extends south to the E1D/E1E discontinuity. Two smaller areas of domes occur in the middle of segment E1E. Segment E2 has the V-shaped bathymetric profile and low inflation characteristic of reduced magma supply ridges [*Macdonald and Fox*, 1983], yet few areas of domes are seen along this segment, including near both the northern and southern tips and a few domes near the center of the segment. Other than a very small area near the northern tip of segment E3, this segment is free of domes, although a third-order discontinuity occurs near 31°S. The next area with a few domes occurs near the northern tip of segment E4. There are also a few domes near the southern end of this segment where it curves into a large OSC.

[69] Thus the clear correlation that *White et al.* [2002a] found between lava domes and third-order discontinuities at 9–10°N is not seen at these faster rates, but there is a fairly good correlation between domes and second-order discontinuities.

8. Conclusions

[70] The part of the East Pacific Rise spreading faster than 142 km/Myr is presently behaving fundamentally differently than the part spreading slower than 136 km/Myr. The slower spreading part has the more classic ridge-transform geometry, while the faster spreading part is reorganizing by propagating rifts and microplate tectonics. The boundary between fast and superfast spreading behavior as defined this way presently occurs somewhere between the fastest-slipping (Garrett) transform at 13°S and the dueling propagators near 21°S.

[71] Large-scale fracturing patterns observed in the DSL-120 kHz side-scan data define natural segmentation scales along the fastest spreading ridge segments. These usually, but not always, correlate with linear volcanic systems in the SeaBeam data. These structural patterns indicate that some subsegments are behaving cohesively, with in-phase tectonic activity, while fundamental discontinuities occur between other subsegments, suggesting that the surficial fracture patterns result from different processes than the larger-scale segmentation.

[72] We report the first rigorous correlation between coregistered hydrothermal plume and marine geophysical data on similar scales and over multi-segment distances. In general, the most inflated parts of both the West ridge (on segment W3) and the East ridge (on segment E4) correlate with the most intense and extensive hydrothermal signals on these axes and are both presently in eruptive phases, as shown by voluminous acoustically dark young sheet flows resulting from fissure eruptions. On the West ridge, the two strongest particulate hydrothermal plumes, near 27°42′S and 28°S, occur within 10 km of the two largest areas of dark flows, and the strongest particulate hydrothermal area on the East ridge, near 31°48′S, overlies the highest density dark flow area. Major plume concentrations, especially on the East ridge, were usually found where fracture and fissure density was near zero or at a local minimum. The frequent occurrence of plumes in segment overlap areas suggests that these areas are not magma starved. More of the major plume areas are found near segment ends than near segment centers.

[73] These several correlations suggest that magma (heat) supply, rather than crustal permeability, is the primary control on hydrothermal venting in this area. The most effective strategy in the search for active venting at these spreading rates is thus to target local axial inflation maxima where fracture density is low and young lava flows are prominent.

[74] We agree with *Wright et al.* [2002] that there appear to be important differences between fast and superfast patterns of fracturing and hydrothermal discharge. Thus while comprehensive studies of particular locations (e.g., the 9–10°N RIDGE ISS site) are important, it is equally important to expand such work to mid-ocean ridges at various spreading rates, where the balance between heat supply and permeability in controlling hydrothermal patterns may be surprisingly different.

Acknowledgments

[75] We thank Captain Curl and the R/V *Melville* crew and the entire WHOI DSL group, especially D. Gleason, S. Gegg, and T. Crook, and S. Maenner for superb help at sea. A. Bowen, D. Fornari, and D. Scheirer provided valuable help in planning the expedition. We thank T. Reed, A. Andersson, and the OIC group for help reprocessing the DSL bathymetry data, P. Johnson for help processing the SeaBeam data, and N. Hulbirt, V. Nakahara, and D. Dale for assistance. Useful

reviews by D. Fornari and C. German improved the paper, as did comments from R. Haymon, K. Macdonald, and S. Rowland. We thank the government of Chile for permitting work in their territorial waters near Easter Island. This material is based upon work supported by the National Science Foundation under grants OCE-9529737 and OCE-9906896 and by the NOAA Vents Program. SOEST contribution 6400, PMEL contribution 2707, JISAO contribution 1075.

References

Anderson-Fontana, S., J. F. Engeln, P. Lundgren, R. L. Larson, and S. Stein (1986), Tectonics and evolution of the Juan Fernandez microplate at the Pacific-Nazca-Antarctic triple junction, *J. Geophys. Res.*, *91*, 2005–2018.

Baker, E. T., and T. Urabe (1996), Extensive distribution of hydrothermal plumes along the superfast-spreading East Pacific Rise, 13°50′–18°40′S, *J. Geophys. Res.*, *101*, 8685–8695.

Baker, E. T., Y. J. Chen, and J. Phipps Morgan (1996), The relationship between near-axis hydrothermal cooling and the spreading rate of midocean ridges, *Earth Planet. Sci. Lett.*, *142*, 137–145.

Baker, E. T., D. A. Tennant, R. A. Feely, G. T. Lebon, and S. L. Walker (2001), Field and laboratory studies on the effect of particle size and composition on optical backscattering measurements in hydrothermal plumes, *Deep Sea Res., Part I*, *48*, 593–604.

Baker, E. T., et al. (2002), Hydrothermal venting along Earth's fastest spreading center: East Pacific Rise, 27.5°–32.3°, *J. Geophys. Res.*, *107*(B7), 2130, doi:10.1029/2001JB000651.

Batiza, R. (1996), Magmatic segmentation of mid-ocean ridges: A review, in *Tectonic, Magmatic, Hydrothermal and Biological Segmentation of Mid-Ocean Ridges*, edited by C. J. MacLeod, P. A. Tyler, and C. L. Walker, *Geol. Soc. Spec. Publ.*, *118*, 103–130.

Batiza, R., and S. H. Margolis (1986), Small non-overlapping offsets of the East Pacific Rise, *Nature*, *320*, 439–441.

Bird, R. T., and D. F. Naar (1994), Intratransform origins of mid-ocean ridge microplates, *Geology*, *22*, 987–990.

Bird, R. T., D. F. Naar, R. L. Larson, R. C. Searle, and C. R. Scotese (1998), Plate tectonic reconstructions of the Juan Fernandez microplate: Transformation from internal shear to rigid rotation, *J. Geophys. Res.*, *103*, 7049–7067.

Bohnenstiehl, D. R., and S. M. Carbotte (2001), Faulting patterns near 19°30′S on the East Pacific Rise: Fault formation and growth at a superfast spreading center, *Geochem. Geophys. Geosyst.*, *2*, doi:10.1029/2001GC000156.

Bohnenstiehl, D. R., and M. C. Kleinrock (1999), Faulting and fault scaling on the median valley floor of the TAG segment, 26°N, Mid-Atlantic Ridge, *J. Geophys. Res.*, *104*, 29,351–29,364.

Carbotte, S. M., W. B. F. Ryan, W. Jin, M. Cormier, E. Bergmanis, J. Sinton, and S. White (2003), Magmatic subsidence of the East Pacific Rise (EPR) at 18°14′S revealed through fault restoration of ridge crest bathymetry, *Geochem. Geophys. Geosyst.*, *4*, 1008, doi:10.1029/2002GC000337.

Chadwick, W. W.Jr., D. S. Scheirer, R. W. Embley, and H. P. Johnson (2001), High-resolution bathymetric surveys using scanning sonars: Lava flow morphology, hydrothermal vent and geologic structure at recent eruption sites on the Juan de Fuca Ridge, *J. Geophys. Res.*, *106*, 16075–16100.

Cormier, M.-H., and K. C. Macdonald (1994), East Pacific Rise 18°S–19°S: Asymmetric spreading and ridge reorientation by ultra-fast migration of ridge axis discontinuities, *J. Geophys. Res.*, *99*, 543–564.

Cormier, M.-H., W. B. F. Ryan, A. K. Shah, W. Jin, A. M. Bradley, and D. R. Yoerger (2003), Waxing and waning volcanism along the East Pacific Rise on the millennium time scale, *Geology*, *31*, 633–636.

DeMets, C., R. G. Gordon, D. F. Argus, and S. Stein (1990), Current plate motions, *Geophys. J. Int.*, *101*, 425–478.

DeMets, C., R. G. Gordon, D. F. Argus, and S. Stein (1994), Effect of recent revisions to the geomagnetic reversal time scale on estimates of current plate motions, *Geophys. Res. Lett.*, *21*, 2191–2194.

Edwards, M. H., D. J. Fornari, A. Malinverno, W. B. F. Ryan, and J. Madsen (1991), The regional tectonic fabric of the East Pacific Rise from 12°50′N to 15°10′N, *J. Geophys. Res.*, *96*, 7995–8017.

Engels, J. L., M. H. Edwards, D. J. Fornari, M. R. Perfit, and J. R. Cann (2003), A new model for submarine volcanic collapse formation, *Geochem. Geophys. Geosyst.*, *4*, 1077, doi:10.1029/2002GC000483.

Fornari, D. J., and R. W. Embley (1995), Tectonic and volcanic controls on hydrothermal processes at the mid-ocean ridge: An overview based on near-bottom and submersible studies, in *Physical, Chemical, Biological, and Geological Interactions within Seafloor Hydrothermal Systems*, *Geophys. Monogr. Ser.*, vol. 91, edited by S. E. Humphris et al., pp. 1–46, AGU, Washington, D. C.

Fornari, D. J., R. M. Haymon, M. R. Perfit, T. K. P. Gregg, and M. H. Edwards (1998), Axial summit trough of the East Pacific Rise 9°–10°N: Geological characteristics and evolution of the axial zone on fast spreading mid-ocean ridges, *J. Geophys. Res.*, *103*, 9827–9855.

Fornari, D., et al. (2004), Submarine lava flow emplacement at the East Pacific Rise 9°50′N: Implications for uppermost ocean crust stratigraphy and hydrothermal fluid circulation, in *Mid-Ocean Ridges: Hydrothermal Interactions Between the Lithosphere and Oceans*, *Geophys. Monogr. Ser.*, AGU, Washington, D. C., in press.

Forsyth, D. W. (1992), Geophysical constraints on mantle flow and melt generation beneath mid-ocean ridges, in *Mantle Flow and Melt Generation at Mid-Ocean Ridges*, *Geophys. Monogr. Ser.*, vol. 71, edited by J. Phipps Morgan, D. K. Blackman, and J. M. Sinton, pp. 1–65, AGU, Washington, D. C.

Fox, P. J., and D. G. Gallo (1984), A tectonic model for ridge-transform-ridge plate boundaries: Implications for the structure of oceanic lithosphere, *Tectonophysics*, *104*, 205–242.

German, C. R., L. M. Parson, and the HEAT Scientific Team (1996), Hydrothermal exploration near the Azores triple junction: Tectonic control of venting at slow spreading ridges?, *Earth Planet. Sci. Lett.*, *138*, 93–104.

Gregg, T. K., and D. J. Fornari (1998), Long submarine lava flows: Observations and results from numerical modeling, *J. Geophys. Res.*, *103*, 27,517–27,531.

Griffiths, R. W., and J. H. Fink (1992), Solidification and morphology of submarine lavas: A dependence on extrusion rate, *J. Geophys. Res.*, *97*, 19,729–19,737.

Hanan, B. B., and J. G. Schilling (1989), Easter microplate evolution: Pb isotope evidence, *J. Geophys. Res.*, *94*, 7432–7448.

Haymon, R. M. (1996), The response of ridge-crest hydrothermal systems to segmented, episodic magma supply, in *Tectonic, Magmatic, Hydrothermal and Biological Segmentation of Mid-Ocean Ridges*, edited by C. J. MacLeod, P. A. Tyler, and C. L. Walker, *Geol. Soc. Spec. Publ.*, *118*, 157–168.

Haymon, R. M., D. J. Fornari, M. H. Edwards, S. Carbotte, D. Wright, and K. C. Macdonald (1991), Hydrothermal vent distribution along the East Pacific Rise crest (9°09′–54′N) and its relationship to magmatic and tectonic processes on fast-spreading mid-ocean ridges, *Earth Planet. Sci. Lett.*, *104*, 513–534.

Haymon, R. M., et al. (1993), Volcanic eruption of the mid-ocean ridge along the East Pacific Rise at 9°45–52′N: Direct submersible observation of seafloor phenomena associated with an eruption event in April, 1991, *Earth Planet. Sci. Lett.*, *119*, 85–101.

Hey, R. N. (1977), A new class of pseudofaults and their bearing on plate tectonics: A propagating rift model, *Earth Planet. Sci. Lett.*, *37*, 321–325.

Hey, R. N., F. K. Duennebier, and W. J. Morgan (1980), Propagating rifts on mid-ocean ridges, *J. Geophys. Res.*, *85*, 3647–3658.

Hey, R. N., D. F. Naar, M. C. Kleinrock, W. J. Phipps Morgan, E. Morales, and J. G. Schilling (1985), Microplate tectonics along a superfast seafloor spreading system near Easter Island, *Nature*, *317*, 320–325.

Hey, R. N., M. C. Kleinrock, S. P. Miller, T. M. Atwater, and R. C. Searle (1986), Sea Beam/Deep-Tow investigation of an active oceanic propagating rift system, *J. Geophys. Res.*, *91*, 3369–3393.

Hey, R. N., P. D. Johnson, F. Martinez, J. Korenaga, M. L. Somers, Q. J. Huggett, T. P. LeBas, R. I. Rusby, and D. F. Naar (1995), Plate boundary reorganization at a large-offset, rapidly propagating rift, *Nature*, *378*, 167–170.

Hilgen, F. J. (1991), Astronomical calibration of Gauss to Matuyama sapropels in the Mediterranean and implication for the geomagnetic polarity time scale, *Earth Planet. Sci. Lett.*, *104*, 226–244.

Hooft, E. E. E., R. S. Detrick, and G. M. Kent (1997), Seismic structure and indicators of magma budget along the southern East Pacific Rise, *J. Geophys. Res.*, *102*, 27,319–27,340.

Johnson, P. J. (1996), Recent structural evolution of the East Pacific Rise 29°S large-scale dueling propagator system, M.S. thesis, Univ. of Ha. at Manoa, Honolulu.

Klaus, A., W. Icay, D. F. Naar, and R. N. Hey (1991), Sea-MARC II survey of a propagating limb of a large non-transform offset near 29°S along the fastest spreading East Pacific Rise segment, *J. Geophys. Res.*, *96*, 9985–9998.

Kleinrock, M. C., R. C. Searle, and R. N. Hey (1989), Tectonics of the failing spreading system associated with the 95.5°W Galapagos propagator, *J. Geophys. Res.*, *94*, 13,839–13,858.

Korenaga, J., and R. N. Hey (1996), Recent dueling propagation history at the fastest spreading center, the East Pacific Rise, 26°–32°S, *J. Geophys. Res.*, *101*, 18,023–18,041.

Langmuir, C. H., J. F. Bender, and R. Batiza (1986), Petrologic and tectonic segmentation of the East Pacific Rise, 5°30′–14°30′N, *Nature*, *322*, 422–429.

Larson, R. L., R. C. Searle, M. C. Kleinrock, H. Schouten, R. T. Bird, D. F. Naar, R. I. Rusby, E. E. Hooft, and H. Lasthiotakis (1992), Roller-bearing tectonic evolution of the Juan Fernandez microplate, *Nature*, *356*, 571–576.

Lonsdale, P. (1983), Overlapping rift zones at the 5.5°S offset of the East Pacific Rise, *J. Geophys. Res.*, *88*, 9393–9406.

Lonsdale, P. (1989), Segmentation of the Pacific-Nazca spreading center, 1°N–20°S, *J. Geophys. Res.*, *94*, 12,197–12,225.

Lupton, J., D. Butterfield, M. Lilley, J. Ishibashi, D. Hey, and L. Evans (1999), Gas chemistry of hydrothermal fluids along the East Pacific Rise, 5°S to 32°S (abstract), *Eos Trans. AGU*, *80*(46), Fall Meet. Suppl., F1099.

Macdonald, K. C., and P. J. Fox (1983), Overlapping spreading centers: New accretion geometry of the East Pacific Rise, *Nature*, *301*, 55–58.

Macdonald, K. C., and P. J. Fox (1988), The axial summit graben and cross-sectional shape of the East Pacific Rise as indicators of axial magma chambers and recent volcanic eruptions, *Earth Planet. Sci. Lett.*, *88*, 119–131.

Macdonald, K. C., J. C. Sempere, P. J. Fox, and R. Tyce (1987), Tectonic evolution of ridge axis discontinuities by the meeting, linking, or self-decapitation of neighboring ridge segments, *Geology*, *15*, 993–997.

Macdonald, K. C., R. M. Haymon, S. P. Miller, J.-C. Sempere, and P. J. Fox (1988a), Deep-Tow and Sea Beam studies of dueling propagating ridges on the East Pacific Rise near 20°40′S, *J. Geophys. Res.*, *93*, 2875–2898.

Macdonald, K. C., P. J. Fox, L. J. Perram, M. F. Eisen, R. M. Haymon, S. P. Miller, S. M. Carbotte, M.-H. Cormier, and A. N. Shor (1988b), A new view of the mid-ocean ridge from the behavior of ridge-axis discontinuities, *Nature*, *335*, 217–225.

Macdonald, K. C., D. S. Scheirer, and S. M. Carbotte (1991), Mid-ocean ridges: Discontinuities, segments and giant cracks, *Science*, *253*, 986–994.

Martinez, F., R. N. Hey, and P. D. Johnson (1997), The East ridge system 28.5–32°S East Pacific Rise: Implications for overlapping spreading center development, *Earth Planet. Sci. Lett.*, *151*, 13–31.

Massoth, G. J., E. T. Baker, R. A. Feely, J. E. Lupton, R. W. Collier, J. F. Gendron, K. K. Roe, S. M. Maenner, and J. A. Resing (1998), Manganese and iron in hydrothermal plumes resulting from the 1996 Gorda Ridge Event, *Deep Sea Res., Part II*, *45*, 2683–2712.

Montelli, R., G. Nolet, F. A. Dahlen, G. Masters, E. R. Engdahl, and S.-H. Hung (2004), Finite frequency tomography reveals a variety of plumes in the mantle, *Science*, *303*, 338–343.

Naar, D. F., and R. N. Hey (1986), Fast rift propagation along the East Pacific Rise near Easter Island, *J. Geophys. Res.*, *91*, 3425–3438.

Naar, D. F., and R. N. Hey (1989a), Speed limit for oceanic transform faults, *Geology*, *17*, 420–422.

Naar, D. F., and R. N. Hey (1989b), Recent Pacific-Easter-Nazca plate motions, in *Evolution of Mid-Oceanic Ridges*, *Geophys. Monogr. Ser.*, vol. 57, pp. 9–30, AGU, Washington, D. C.

Naar, D. F., and R. N. Hey (1991), Tectonic evolution of the Easter Microplate, *J. Geophys. Res.*, *96*, 7961–7993.

Pardee, D. R., R. N. Hey, and F. Martinez (2000), Cross-sectional areas of mid-ocean ridge axes bounding the Easter and Juan Fernandez Microplates, *Mar. Geophys. Res.*, *20*, 517–531.

Phipps Morgan, J., and E. M. Parmentier (1985), Causes and rate-limiting mechanisms of ridge propagation: A fracture mechanics model, *J. Geophys. Res.*, *90*, 8603–8612.

Pollard, D. D., and A. Aydin (1984), Propagation and linkage of oceanic ridge segments, *J. Geophys. Res.*, *89*, 10,017–10,028.

Poreda, R. J., J.-G. Schilling, and H. Craig (1993), Helium isotope ratios in Easter microplate basalts, *Earth Planet. Sci. Lett.*, *119*, 319–329.

Rusby, R. I., and R. C. Searle (1995), A history of the Easter Microplate, 5.25 Ma to present, *J. Geophys. Res.*, *100*, 12,617–12,640.

Scheirer, D. S., and K. C. Macdonald (1993), Variation in cross-sectional area of the axial ridge along the East Pacific

Rise: Evidence for the magmatic budget of a fast-spreading center, *J. Geophys. Res.*, *98*, 7871–7885.

Scheirer, D. S., D. J. Fornari, S. E. Humphris, and S. Lerner (2000), High-resolution seafloor mapping using the DSL-120 sonar system: Quantitative assessment of sidescan and phase-bathymetry data from the Lucky Strike segment of the Mid-Atlantic ridge, *Mar. Geophys. Res.*, *21*, 121–142.

Schilling, J. G., H. Sigurdsson, A. Davis, and R. N. Hey (1985), Easter microplate evolution, *Nature*, *317*, 325–331.

Searle, R. C. (1983), Multiple, closely spaced transform faults in fast-slipping fracture zones, *Geology*, *11*, 607–610.

Searle, R. C., R. I. Rusby, J. Engeln, R. N. Hey, J. Zukin, P. M. Hunter, T. P. LeBas, H.-J. Hoffman, and R. Livermore (1989), Comprehensive sonar imaging of the Easter microplate, *Nature*, *341*, 701–705.

Sempere, J. C., and K. C. Macdonald (1986), Overlapping spreading centers: Implications from crack growth simulation by the displacement discontinuity method, *Tectonics*, *5*, 151–163.

Shackleton, N. J., A. Berger, and W. R. Peltier (1990), An alternative astronomical calibration of the lower Pleistocene timescale based on ODP site 677, *Trans. R. Soc. Edinburgh Earth Sci.*, *81*, 251–261.

Stewart, W. K., D. Chu, S. Malik, S. Lerner, and H. Singh (1994), Quantitative seafloor characterization using a bathymetric sidescan sonar, *IEEE J. Oceanic Eng.*, *19*, 599–610.

Walker, S. L., E. T. Baker, G. Massoth, and R. N. Hey (2004), Short-term variations in the distribution of hydrothermal plumes along a superfast spreading center, East Pacific Rise, 27°30′–32°20′S, *Geochem. Geophys. Geosyst.*, *5*, Q12005, doi:10.1029/2004GC000789.

Wetzel, L. R., D. A. Wiens, and M. C. Kleinrock (1993), Evidence from earthquakes for bookshelf faulting at large non-transform ridge offsets, *Nature*, *362*, 235–237.

White, S. M., K. C. Macdonald, and R. M. Haymon (2000), Basaltic lava domes, lava lakes, and volcanic segmentation on the southern East Pacific Rise, *J. Geophys. Res.*, *105*, 23,519–23,536.

White, S. M., R. M. Haymon, D. J. Fornari, M. R. Perfit, and K. C. Macdonald (2002a), Correlation between volcanic and tectonic segmentation of fast-spreading ridges: Evidence from volcanic structures and lava flow morphology on the East Pacific Rise at 9°–10°N, *J. Geophys. Res.*, *107*(B8), 2173, doi:10.1029/2001JB000571.

White, S. M., K. C. Macdonald, and J. M. Sinton (2002b), Volcanic mound fields on the East Pacific Rise, 16°–19°S: Low effusion rate eruptions at overlapping spreading centers for the past 1 Myr, *J. Geophys. Res.*, *107*(B10), 2240, doi:10.1029/2001JB000483.

Wilson, D. S. (1996), Fastest known spreading on the Miocene Cocos-Pacific plate boundary, *Geophys. Res. Lett.*, *23*, 3003–3006.

Won, Y., C. R. Young, R. A. Lutz, and R. C. Vrijenhoek (2003), Dispersal barriers and isolation among deep-sea mussel populations (Mytilidae:*Bathymodiolus*) from eastern Pacific hydrothermal vents, *Mol. Ecol.*, *12*, 169–184.

Wright, D. J., R. M. Haymon, and D. J. Fornari (1995a), Crustal fissuring and its relationship to magmatic and hydrothermal processes on the East Pacific Rise crest (9°12′–54′N), *J. Geophys. Res.*, *100*, 6097–6120.

Wright, D. J., R. M. Haymon, and K. C. Macdonald (1995b), Breaking new ground: Estimates of crack depth along the axial zone of the East Pacific Rise (9°12–54′N), *Earth Planet. Sci. Lett.*, *134*, 441–457.

Wright, D. J., R. M. Haymon, S. M. White, and K. C. Macdonald (2002), Crustal fissuring on the crest of the southern East Pacific Rise at 17°15′–40′S, *J. Geophys. Res.*, *107*(B5), 2104, doi:10.1029/2001JB000544.